Optimization Design Method of Tendon-Sheath Transmission Path Under Curvature Constraint

Yanan Li, Weining Lu, Yu Liu, Deshan Meng, *Member, IEEE*, Xueqian Wang, and Bin Liang

***Abstract*—The application requirements of the tendon-sheath mechanism in the field of precision machinery are becoming increasingly extensive. However, the contact friction between the tendon and sheath seriously affects the transmission accuracy. In the case of unavoidable friction, optimizing the tendon transmission path to reduce tension loss and elastic deformation has become an important research direction. In this article, the influence law of the tendon transmission path on the tension and displacement transmission is obtained using the two parameters related to the curvature of the transmission path: total bending angle and equivalent tendon length. Then, based on the optimal control theory and minimum principle, the different transmission path solutions of the minimum tension loss, the minimum tendon deformation, and the coupling of tension and displacement are obtained; the numerical optimization method verifies the correctness of the proposed theory. Finally, an optimal design of a tendon-constrained synchronous rotation mechanism for the manipulator is carried out, and the linkage performance is greatly improved by optimizing the transmission path.**

***Index Terms*—Curvature constraint, optimal control, synchronous rotation mechanism, tendon-sheath, transmission path.**

I. Introduction

TENDON-SHEATH transmission, also known as cable-conduit transmission, is intended to imitate the working principle of human musculoskeletal. Owing to its advantages of small transmission module mass, long transmission distance, and simple wiring configuration, it has been widely used in wearable devices [1], surgical robots [2], and soft robots [3].

However, there is a distributed friction effect between the tendon and the sheath, which makes the tendon tension in the contact parts unevenly distributed. Hence, the tendon tension at the input and output ends is significantly attenuated. In addition, tendon stiffness is limited. The change of tendon tension during the pulling process causes elastic deformation, and the displacement transmission has hysteresis phenomena, which challenges precise control.

TABLE I
Transmission Performance Impact Analysis

Factors	Terms	Description
Tendon	Stiffness	Steel wire [7], Nylon tendon [8]
	Slack effect	Preload [9]: prevent tendon slack
Sheath	Stiffness	Bowden cable [9], Teflon tube [10]
	Path constraint	Anchor points [11], Arm of force [12]
		Attachment points [13]
Coupling	Friction	Relative friction coefficient [14], [15]
		Relative radius (gap) [14], [16]
		Relative velocity [17]

To improve transmission performance, a series of researches on tendon-sheath force and motion compensation control have been carried out, such as model-based feedforward control [4], feedback control [5], and nonmodel-based control [6]. These control methods usually assume that the sheath shape is known and compensate for the desired output by identifying system parameters or feedback control. The current research on improving transmission performance is also concentrated on this aspect. However, improving the transmission performance by means of compensation faces the situation of limited sensing, for example, sensors sometimes cannot be installed at the remote end. In contrast, it requires additional energy consumption of the system, which is detrimental to the transmission. If the transmission can be optimized in design, the transmission performance can be improved at the root.

The main factors that affect the design of the tendon-sheath mechanism are shown in Table I. The following parameters are usually considered: sheath length, friction coefficient, bending radius, preload, tendon elasticity, etc. [16]. The factors affecting the transmission were found through experiments combining nine variables [15]. However, there are many variables and combinations involved, and it is difficult to consider them comprehensively. Also, the conclusions are limited owing to the lack of theoretical guidance. Recently, the optimization of the flow path of the soft pneumatic actuator has brought inspiration, Joshi et al. [18] optimized the pipe diameter and length to achieve the best performance and portability. By summarizing

Manuscript received 6 October 2022; revised 5 February 2023; accepted 25 February 2023. Date of publication 29 March 2023; date of current version 8 August 2023. This work was supported in part by the National Key R&D Program of China under Grant 2022YFB4701400/4701402, in part by the National Natural Science Foundation of China under Grant 61903215 and Grant U1813216, and in part by Guangdong Natural Science Foundation under Grant 2022A1515010543. This paper was recommended for publication by Associate Editor P. Renaud and Editor M. Yim upon evaluation of the reviewers' comments. *(Corresponding authors: Yu Liu; Deshan Meng.)*

Yanan Li and Yu Liu are with the Harbin Institute of Technology, Harbin 150000, China (e-mail: 19b308004@stu.hit.edu.cn; lyu11@hit.edu.cn).

Weining Lu and Bin Liang are with the Department of Automation, Tsinghua University, Beijing 100084, China (e-mail: luwn@tsinghua.edu.cn; liangbin@mail.tsinghua.edu.cn).

Deshan Meng is with the School of Aeronautics and Astronautics, Sun Yat-Sen University, Shenzhen 518107, China (e-mail: mengdsh3@mail.sysu.edu.cn).

Xueqian Wang is with Shenzhen International Graduate School, Tsinghua University, Shenzhen 518055, China (e-mail: wang.xq@sz.tsinghua.edu.cn).

Color versions of one or more figures in this article are available at https://doi.org/10.1109/TRO.2023.3255545.

Digital Object Identifier 10.1109/TRO.2023.3255545

IEEE Transactions on Robotics (T-RO) paper, presented at ICRA 2024, Yokohama, Japan. Cite as T-RO paper.

the abovementioned design process, the transmission design can be divided into transmission model analysis, optimization problem description, and transmission path design.

The tendon-sheath transmission model is essentially a process of calculating the nonuniformly distributed tension caused by friction and elastic deformation of the tendon. Kaneko et al. [19] established the basic transmission model of the tendon-sheath and proposed the concept of characterizing stiffness. The concept of accumulated curve angle is proposed in [20]; the tension attenuation is directly related to the accumulated curve angle. Furthermore, the deformation of the tendon can be obtained by the distribution of the tendon tension. Tian et al. [21] pointed out that the force transmission of the tendon-sheath depends on the total bending angle and friction coefficient. Through the analysis of the transmission model, the main factors affecting the transmission are the relative friction coefficient and arrangement of the transmission path. The friction coefficient can be reduced by selecting different contact materials or adding lubricant. However, the available materials are limited, and the choice of the tendon should not only meet tensile strength requirements but also include temperature range and abrasion resistance [8].

While the design of the transmission path only needs to control the shape of the sheath, which is easy to implement. In practical application, the tendon transmission must follow certain path constraints. The term "path constraint" is defined as a mechanical structure that provides constraints on the tendon and prevents it from deviating from a predesigned path [11]. Path constraints include anchor points and attachment points. The anchor points determine the tendon's start and endpoints. The moment arm of the tendon relative to the joint is determined by the position of the anchor point and direction of the tendon. Attachment points are the set of all waypoints connecting the anchor points. The most attractive part of the tendon-sheath system is its mobility and flexibility. Therefore, the transmission path is time-varying in many applications. However, it is not entirely free, for example, there are a series of intermediate anchor points to constrain the sheath [see Fig. 1(a)], or only part of the transmission path is time-varying [see Fig. 1(b) and (c)], such robots include the exosuit [22], [23], [24], [25], the exoglove [1], and many other tendon-driven robots [26], [27], [28], [29], [30]. Therefore, the transmission path can be designed segmentally according to these intermediate points or only optimize part of the transmission path. Hence, the transmission path optimization problem can be abstracted as, given the position and direction of two points, satisfying the curvature constraint, taking the minimum tension attenuation or the minimum tendon deformation as the optimization goal, optimizing the sheath path to improve the transmission performance.

However, to date, no attempt has been made to analyze tendon transmission path design in a systematic manner.

1) Some existing studies point out that tension transmission mainly depends on the total bending angle. However, there is no relevant literature on designing the transmission path to minimize the total bending angle. Previous studies directly assumed that the sheath curvature was known or adopted constant curvature [31] and average curvature [32] models.

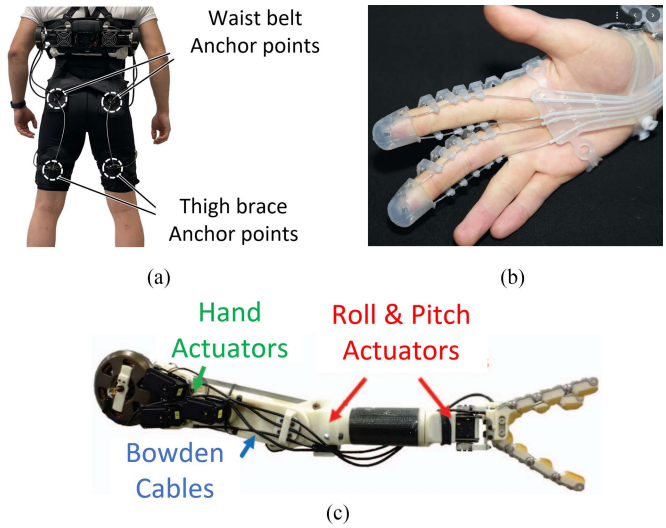

Fig. 1. Tendon-sheath transmission path. (a) Exosuit [24], with intermediate anchor points at the waist belt. (b) Exoglove [1], the finger part transmission path changes, and the palm part transmission path is fixed. (c) Arm of the HERMES humanoid robot [27], the transmission path in the arm is fixed and only changes at the joint.

2) The optimal design of the transmission path is often based on experience or intuition and has not been proven theoretically; for example, the routing of the tendon-sheath drive path is optimized by keeping the geometric envelope on a straight line [21].
3) The transmission path design only considers the transmission process from the active end to the passive end. It does not include the reverse transmission path when the passive end interacts with the environment [33].
4) The two optimization objectives of tension transmission and tendon deformation are often separated, or only one optimization objective is considered. There is no systematic theoretical guidance on designing the sheath path to improve the overall transmission performance in terms of the relationship between the two optimization objectives. For example, the loop routing method was proposed to compensate for friction [13], which ensures that the total bending angle remains unchanged when the end effector is translated. However, it can only guarantee the transfer model of tension, and the displacement transfer model still changes, artificially increasing the friction. Similarly, Sun et al. [34] analyzed the effect of path configuration on tendon elongation by introducing an additional curve on the input side; the effect of the change in sheath configuration on tendon elongation is reduced.

Here, two parameters related to the transmission path are obtained through the analysis of the transmission model. At the same time, the transmission path needs to meet certain curvature constraints. The transmission path design is transformed into an optimal control problem, the research on the tendon transmission path's design method is carried out. The main contributions of this study are as follows.

Based on the optimal control theory and the minimum principle, this study systematically expounds on the theoretical design

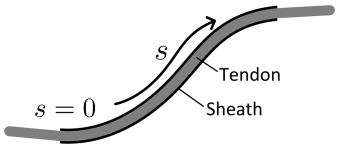

Fig. 2. Schematic of the tendon-sheath transmission.

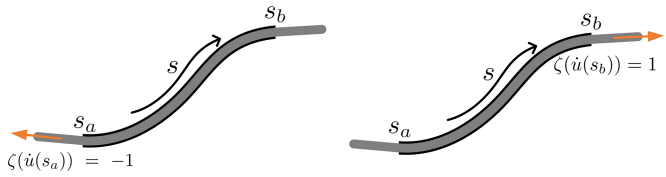

(a) (b)

Fig. 3. Pull the tendon on a different side. (a) Tension on s_a side is used as input, then $\lambda_a = \exp(\mu_c \zeta(\dot{u}(s_a))(\theta(s_b) - \theta(s_a)))$. (b) Tension on s_b side is used as input, then $\lambda_b = \exp(\mu_c \zeta(\dot{u}(s_b))(\theta(s_a) - \theta(s_b)))$.

of the transmission path of the tendon-sheath mechanism: For tension transmission, the total bending angle reflects the overall bending degree of the tendon; therefore, the minimum total bending angle is taken as the goal, and the solution set of the transmission path with the minimum tension loss is obtained. For displacement transmission, owing to the nonuniform distribution of tension on the transmission path caused by friction, the deformation is equal to the deformation of a tendon with an equivalent length without friction attenuation. Therefore, the equivalent tendon length of the friction path is minimized as the goal, and the solution set of the minimum tendon deformation path is obtained. Because the tension and motion transmissions are not isolated, the minimum tendon deformation path is searched based on the priority of tension transmission. Finally, the tendon-constrained synchronous rotation mechanism is improved based on the proposed transmission path design method.

The rest of this article is organized as follows. Section II presents the problem formulation, which mainly includes transmission analysis and optimization problem definition. Section III introduces the minimum principle and Dubins path concept. Then, it presents the solution set of the minimum tension loss path and the minimum tendon deformation path. Section IV provides the solution set of coupling tension and deformation and the relationship between different solution sets, which is verified using the numerical optimization method. In Section V, based on the proposed method, the optimal design of a tendon-constrained synchronous rotation mechanism is presented. Finally, Section VI concludes the article.

II. Problem Formulation

Before proceeding to the problem description, the tendon sheath's force and displacement transmission model was first established, and detailed derivations can be found in [31].

A schematic of the tendon-sheath transmission is shown in Fig. 2, the arc length s is used as the parameter variable, the input–output transfer relationship is

$$T(s_{\text{out}}) = T(s_{\text{in}}) \exp\left(\mu_c \int_{s_{\text{in}}}^{s_{\text{out}}} \text{sign}(\dot{u}(s))k(s)ds\right)$$

$$u(s_{\text{out}}) - u(s_{\text{in}}) = \frac{T(s_{\text{in}})}{EA} \int_{s_{\text{in}}}^{s_{\text{out}}} \exp\left(\mu_c \int_{s_{\text{in}}}^{s} \text{sign}(\dot{u}(\ell))k(\ell)d\ell\right) ds \quad (1)$$

where, s_{in} and s_{out} are the arc lengths of the input and output sides, $T(\cdot)$ is the tension along the tendon; $u(\cdot)$ and $\dot{u}(\cdot)$ are the axial displacement and velocity; $\kappa(\cdot)$ is the sheath curvature; $\exp(\cdot)$ and $\text{sign}(\cdot)$ are exponential and sign function; E and A are the elastic modulus and cross-sectional area of the tendon, μ_c is the kinetic friction coefficient.

A. Tension Transmission

The tension input–output relationship determines the force transmission efficiency to the distal end, from (1), the tension transfer coefficient is defined as

$$\lambda = \frac{T(s_{\text{out}})}{T(s_{\text{in}})} = \exp\left(\mu_c \int_{s_{\text{in}}}^{s_{\text{out}}} \text{sign}(\dot{u}(s))k(s)ds\right). \quad (2)$$

A key concept in the transfer model is the cumulative bending angle [20], which reflects the bending degree of the sheath and is defined as the integral of the curvature

$$\theta(s) = \int_0^s k(\ell)d\ell. \quad (3)$$

Assumption 1: If the tendon slides completely in the sheath, the direction of the axial velocity of the tendon at any position in the sheath is the same; that is, for any s, $\text{sign}(\dot{u}(s)) = \text{sign}(\dot{u}(s_{\text{in}}))$, abbreviated as $\zeta(\dot{u}(s_{\text{in}}))$.

Then, the tension transmission coefficient is converted to

$$\lambda = \exp\left(\mu_c \zeta(\dot{u}(s_{\text{in}}))\left(\theta(s_{\text{out}}) - \theta\left(s_{\text{in}}\right)\right)\right). \quad (4)$$

The total bending angle of arc $s_{\text{in}}\widehat{s_{\text{out}}}$ is

$$\Theta_{s_{\text{in}}\widehat{s_{\text{out}}}} = |\theta(s_{\text{out}}) - \theta(s_{\text{in}})| = \left|\int_{s_{\text{in}}}^{s_{\text{out}}} k(s)ds\right|. \quad (5)$$

Suppose s_a, s_b are the arc lengths on both sides of the sheath and $0 = \theta(s_a) < \theta(s_b) = \Theta_{s_a\widehat{s_b}}$ (see Fig. 3), define λ_a^- to indicate that the tendon movement direction is negative, that is, $\zeta(\dot{u}(s_a)) = -1$, similar for λ_b^+, then

$$\lambda_a^- = \lambda_b^+ = \exp\left(-\mu_c \Theta_{s_a\widehat{s_b}}\right). \quad (6)$$

Therefore, the tension transmission is independent of the input side, and the tendon is pulled on either side, which is related only to the value of the total bending angle. Ideally, the tendon tension on the input and output sides is equal, that is, $\lambda = 1$; therefore, the tension transfer optimization objective is equivalent to minimizing the total bending angle

$$\min|\lambda - 1| \equiv \min \Theta_{s_a\widehat{s_b}}. \quad (7)$$

B. Displacement Transmission

The displacement input–output relationship reflects the influence of the tendon deformation on the control accuracy, the displacement transfer coefficient is defined as

$$\gamma = \frac{u(s_{\text{out}})}{u(s_{\text{in}})}. \tag{8}$$

The absolute deformation of the tendon is $\Delta u = u(s_{\text{out}}) - u(s_{\text{in}})$, from (1)

$$\eta = \frac{EA}{T(s_{\text{in}})}\Delta u = \int_{s_{\text{in}}}^{s_{\text{out}}} \exp\left(\mu_c \int_{s_{\text{in}}}^{s} \text{sign}(\dot{u}(\ell))k(\ell)d\ell\right) ds. \tag{9}$$

We defined η as the equivalent tendon length of the frictional transmission path. On a frictionless transmission path, the tendon deformation $\Delta u = \frac{T}{EA}l$ intuitively indicates that the tendon has a uniform tension distribution, and the same tension is applied on one side; the shorter the length, the smaller the deformation. Owing to the nonuniform tension distribution on the frictional transmission path, under the same tension input, the deformation of the tendon is equal to that of the frictionless transmission path with an equivalent tendon length η.

Then, (8) can be transformed into

$$\gamma = \frac{u(s_{\text{in}}) + \Delta u}{u(s_{\text{in}})} = 1 + \frac{1}{EA}\frac{T(s_{\text{in}})}{u(s_{\text{in}})}\eta. \tag{10}$$

The abovementioned equation comprises three parts, of which $\frac{T_{\text{in}}}{u_{\text{in}}}$ is determined by external input. Here, the input was assumed to be the same, and input-related factors were ignored. In addition, E and A depend on the tendon material and cross-sectional area, and only η is related to the transmission path; therefore, the optimization objective of displacement transfer is equivalent to minimizing the equivalent tendon length

$$\min|\gamma - 1| \equiv \min|\eta|. \tag{11}$$

Similarly, when pulling the tendon on different sides, the equivalent tendon length

$$\eta_a^- = \int_{s_a}^{s_b} \exp\left(-\mu_c\left(\theta(s) - \theta\left(s_a\right)\right)\right) ds$$
$$\eta_b^+ = \int_{s_b}^{s_a} \exp\left(\mu_c\left(\theta(s) - \theta\left(s_b\right)\right)\right) ds. \tag{12}$$

That is, when the same force is applied on different sides of the sheath, the equivalent tendon length may be different: $|\eta_a^-| = |\eta_b^+|$ is only available when the cumulative bending angle is symmetrically distributed.

C. Transmission Path Optimization

From the abovementioned transmission analysis, the transmission path design is mainly to optimize the sheath curvature. An excessive wiring curvature is a high-risk factor for robot failure [7]. Therefore, the sheath must satisfy certain curvature constraints. The curvature constraint includes two aspects. First, excessive bending forms creases on the sheath, which greatly increases the friction locally, thus causing the tendon to break. The second is the excessive bending of the tendon; it loops and eventually forms a kink with increasing accumulated twist; thus, the damage is irreversible and easy to break. Therefore, for different tendon and sheath material combinations, the final curvature constraint depends on the tendon's and sheath's relative stiffnesses. For example, the nylon tendon is very soft and can be bent arbitrarily; therefore, the curvature constraint of the sheath plays a major role, and the achievable minimum bend radius can be calculated using estimates of strain at yield [35]. While the steel wire has a certain bending stiffness and the final curvature constraint may depend on the tendon, Table II lists the reference relationship between the tendon diameter and the minimum bending radius.

TABLE II
REFERENCE RELATIONSHIP BETWEEN THE TENDON DIAMETER AND THE MINIMUM BENDING RADIUS

Tendon Diameter (mm)	Minimum Breaking Load (kN)	Pulley Desirable Minimum Bending Radius (mm)	Pulley Critical Minimum Bending Radius (mm)
0.54	0.16	11.5	7.5
0.81	0.37	17	11.5
1	0.56	21	14
1.25	0.88	26.5	17.5

Stainless Steel Cable 7x7.
Standard: BS EN 12385-4:2002+A1:2008.

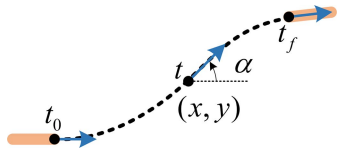

Fig. 4. Particle moves along the transmission path.

Suppose that the sheath's initial position, end position, and orientation are known. Assuming that a particle in the plane moves along the sheath curve at a certain speed $v(t)$, its initial state $\mathbf{p}(0) = [x(0) \quad y(0) \quad \alpha(0)]^T$, the terminal state $\mathbf{p}(t_f) = [x(t_f) \quad y(t_f) \quad \alpha(t_f)]^T$, define $\mathbf{p}(t) = [x(t), y(t), \alpha(t)]^T$ is the state of the particle at any moment t, where $x(t)$, $y(t)$ are the position of the particle, $\alpha(t)$ is the direction angle of the curve (see Fig. 4). Then, the state equation is

$$\dot{\mathbf{p}}(t) = \begin{bmatrix}\dot{x}(t)\\ \dot{y}(t)\\ \dot{\alpha}(t)\end{bmatrix} = v(t)\begin{bmatrix}\cos\alpha(t)\\ \sin\alpha(t)\\ u(t)\end{bmatrix} \tag{13}$$

where, $u(t)$ denotes the control input.

The relationship between the control input and curvature of the curve is

$$u(t) = \frac{\dot{\alpha}(t)}{v(t)} = \frac{1}{v(t)}\frac{d\alpha}{dt} = \frac{d\alpha}{ds} = \text{sign}\left(\frac{d\alpha}{ds}\right)\kappa(t) \tag{14}$$

where, $\kappa(t) = |\frac{d\alpha}{ds}|$ is the curve curvature, $u(t)$ is equal to the curvature, and the sign of $u(t)$ depends on the bending direction of the curve with $\text{sign}(\frac{d\alpha}{ds})$.

The control input satisfies the curvature constraint

$$|u(t)| \le u_{\max} = \kappa_{\max} \tag{15}$$

where, $\kappa_{\max}$ is the maximum curvature, determined by the minimum bending radius.

Because the shape of the transmission path is unrelated to the particle motion speed, without loss of generality, let $v(t) = 1$. The state equations and boundary constraints can be rewritten as

$$\begin{aligned} \dot{x}(t) &= \cos\theta(t) \quad x(0) = x_0 \quad x(t_f) = x_{t_f} \\ \dot{y}(t) &= \sin\theta(t) \quad y(0) = y_0 \quad y(t_f) = y_{t_f} \\ \dot{\alpha}(t) &= u(t) \qquad \alpha(0) = \alpha_0 \quad \alpha(t_f) = \alpha_{t_f}. \end{aligned} \tag{16}$$

For different optimization objectives, the transmission path optimization problem is further defined as follows.

Problem 1: Minimum tension loss path. Under the same tension input, we determine the optimal control input ${}^1u^*$, which minimizes the loss of tension while satisfying the state equation, boundary, and curvature constraints.

Problem 2: Minimum tendon deformation path. Under the same tension input and displacement input, the optimal control input ${}^2u^*$ minimizes the elastic deformation of the tendon and satisfies the state equation, boundary, and curvature constraints.

Problem 3: Coupling transmission path. Considering the influence of tension attenuation and tendon deformation simultaneously, under the same tension output, find the optimal control input ${}^3u^*$ to minimize the elastic deformation of the tendon and satisfy the state equation, boundary, and curvature constraints simultaneously.

The solutions to these problems are presented in Sections III and IV.

III. Minimum Tension Loss and Minimum Tendon Deformation Path

In Section II, (13) and (15) obtain system state equation and input constraints; it can be seen from (1) that both optimization objectives contain integral terms, which can be solved using optimal control theory and the minimum principle.

A. Preliminaries

The system state equation satisfies $\frac{d\mathbf{p}}{dt} = \mathbf{f}(\mathbf{p}(t), \mathbf{u}(t))$, where $\mathbf{p}(t) \in \mathbb{R}^n$ is the state variable, the initial condition $\mathbf{p}(0) = \mathbf{p}_0$, and the termination condition $\mathbf{p}(t_f) = \mathbf{p}_{t_f}$. Control variable $\mathbf{u}(t) : [0, t_f] \in \mathbf{U}$, $\mathbf{U}$ is the control input set, and the cost function is $J(\mathbf{u}) = \int_0^{t_f} f_0(\mathbf{p}(t), \mathbf{u}(t))dt$. The optimal control problem is to determine the optimal control input $\mathbf{u}^*$ under the premise of satisfying the abovementioned constraints to minimize the integral function

$$J(\mathbf{u}^*) = \min_{\mathbf{u}\in\mathbf{U}} J(\mathbf{u}). \tag{17}$$

Define $Q(t) = \int_0^t f_0(\mathbf{p}(\tau), \mathbf{u}(\tau))d\tau$. Then

$$\begin{aligned} \frac{dQ}{dt} &= f_0(\mathbf{p}(t), \mathbf{u}(t)) \\ Q(0) = 0, Q(t_f) &= J(\mathbf{u}). \end{aligned} \tag{18}$$

Let $\bar{\mathbf{p}} = (Q, \mathbf{p}) \in \mathbb{R}^{n+1}$ and $\bar{\mathbf{f}} = (f_0, \mathbf{f})$. Then the optimal control problem is transformed into: for the differential equation $\frac{d\bar{\mathbf{p}}}{dt} = \bar{f}(\bar{\mathbf{p}}, \mathbf{u})$, the initial conditions is $\bar{\mathbf{p}}(0) = (0, \mathbf{p}_0)$, looking for $\mathbf{u} \in \mathbf{U}$, such that the solution of the differential equation satisfies the termination condition: $\bar{\mathbf{p}}(t_f) = (Q(t_f), \mathbf{p}_{t_f})$, meanwhile $Q(t_f) = J(\mathbf{u})$ is guaranteed to be the smallest.

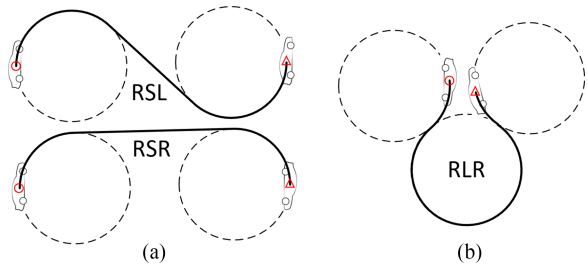

Fig. 5. Form of the Dubins path is related to the relative position of the start and end. When the relative position greater than $4r_{\min}$[38], there must be a CSC type Dubins path, where $r_{\min}$ is the minimum turning radius. (a) There are four forms of RSL, RSR, or LSR, LSL for the CSC path. (b) For the CCC path, there are two forms of RLR or LRL, and the arc length of the middle segment is greater than $\pi r_{\min}$.

Define the costate function $\mathbf{e} \in \mathbb{R}^n$ and constant e_0, let $\bar{\mathbf{e}} = (e_0, \mathbf{e}) \in \mathbb{R}^{n+1}$, the Hamiltonian function is

$$\mathcal{H}(\mathbf{p}, \mathbf{e}, \mathbf{u}) = \bar{\mathbf{e}}\bar{\mathbf{f}} = e_0 f_0(\mathbf{p}, \mathbf{u}) + \mathbf{e}\mathbf{f}(\mathbf{p}, \mathbf{u}). \tag{19}$$

Then, the optimal state $\mathbf{p}^*$ and the optimal costate $\mathbf{e}^*$ satisfy the Hamiltonian Jacobian form

$$\begin{aligned} \frac{d\mathbf{p}}{dt} &= \frac{\partial\mathcal{H}}{\partial\mathbf{e}} \\ \frac{d\mathbf{e}}{dt} &= -\frac{\partial\mathcal{H}}{\partial\mathbf{p}} = -e_0\frac{\partial f_0(\mathbf{p}, \mathbf{u})}{\partial\mathbf{p}} - \mathbf{e}\frac{\partial\mathbf{f}(\mathbf{p}, \mathbf{u})}{\partial\mathbf{p}}. \end{aligned} \tag{20}$$

Minimum Principle [36]: Then, two important conclusions can be obtained, for $\forall t \in [0, t_f]$.

Lemma 1: Optimal control $\mathbf{u}^*(t)$ guarantees that the Hamiltonian function has a global minimum

$$\mathbf{u}^* = \min_{\mathbf{u}\in\mathbf{U}} \mathcal{H}(\mathbf{p}^*, \mathbf{e}^*, \mathbf{u}). \tag{21}$$

Lemma 2: The Hamiltonian function remains constant along the optimal trajectory and, if t_f is free

$$\mathcal{H}(\mathbf{p}^*, \mathbf{e}^*, \mathbf{u}^*) = 0. \tag{22}$$

Dubins path: The set of shortest path solutions in the plane connecting two points, subject to the curvature constraints and the specified initial and end tangent directions. The Dubins path is introduced here because its definition is similar to the transmission path; however, it has different objective functions.

The problem was proposed by Markov in 1889 and solved by Dubins [37] in 1957, providing the first complete solution to the problem and proving that the shortest path connecting two points comprises straight lines and arcs with maximum curvature. The Dubins path solution set is in the form of CSC, CCC, and its subsets, where "S" represents the straight line, and "C" represents the maximum curvature arc. Specifically, according to the direction of rotation, "R" represents the right turn, and "L" represents the left turn (see Fig. 5).

B. Minimum Tension Loss Path

From (3) and (14), the minimum tension loss path objective function is equivalent to minimizing the total bending angle

$$J_1 = \int_0^{L_{en}} \kappa(s)ds = \int_0^{t_f} \left|{}^1u(t)\right|dt. \tag{23}$$

Combining (16), (19), and (23), we define the Hamilton function

$$\begin{aligned}{}^1\mathcal{H}\left(\mathbf{p}(t), {}^1\mathbf{e}(t), {}^1u(t)\right) &= {}^1e_0|{}^1u(t)| + {}^1e_1(t)\cos p_3(t) \\ &\quad + {}^1e_2(t)\sin p_3(t) + {}^1e_3(t){}^1u(t)\end{aligned} \tag{24}$$

where, costate function ${}^1\mathbf{e}(t) = [{}^1e_1(t) \quad {}^1e_2(t) \quad {}^1e_3(t)] \neq \mathbf{0}$ and ${}^1e_0 \geq 0$.

From (20), the optimal costate function ${}^1\mathbf{e}^*(t)$ satisfies

$$\begin{aligned}{}^1\dot{e}_1^*(t) &= 0 \\ {}^1\dot{e}_2^*(t) &= 0 \\ {}^1\dot{e}_3^*(t) &= {}^1e_1^*(t)\sin {}^1p_3^*(t) - {}^1e_2^*(t)\cos {}^1p_3^*(t).\end{aligned} \tag{25}$$

Given that ${}^1e_1^*(t)$ and ${}^1e_2^*(t)$ are constants, ${}^1\dot{e}_3^*(t)$ can be transformed into

$${}^1\dot{e}_3^*(t) = {}^1\rho\sin\left({}^1\alpha^*(t) - {}^1\phi\right) \tag{26}$$

where, ${}^1\rho = \sqrt{({}^1e_1^*(t))^2 + ({}^1e_2^*(t))^2}$, ${}^1\phi = a\tan(\frac{{}^1e_2^*(t)}{{}^1e_1^*(t)})$.

According to the minimum principle, optimize the input ${}^1u(t) \in [-u_{\max}, u_{\max}]$ to minimize the Hamilton function

$${}^1u^*(t) = \quad \arg\min \left({}^1e_0|{}^1u(t)| + {}^1e_3^*(t){}^1u(t)\right). \tag{27}$$

Furthermore, we obtain the optimized input

$$\begin{array}{ll} {}^1u^*(t) = -u_{\max}\,\mathrm{sign}\left({}^1e_3^*(t)\right) & \left|{}^1e_3^*(t)\right| > {}^1e_0 \\ {}^1u^*(t) \in [-u_{\max} \quad 0] & {}^1e_3^*(t) = {}^1e_0 \\ {}^1u^*(t) \in [0 \quad u_{\max}] & {}^1e_3^*(t) = -{}^1e_0 \\ {}^1u^*(t) = 0 & \left|{}^1e_3^*(t)\right| < {}^1e_0. \end{array} \tag{28}$$

According to the value of ${}^1e_0$, there are following two cases.

(1) Abnormal path: When ${}^1e_0 = 0$, the Hamiltonian function is independent of the objective function

$$\begin{aligned}&{}^1\mathcal{H}\left({}^1\mathbf{p}^*(t), {}^1\mathbf{e}^*(t), {}^1u^*(t)\right) \\ &\quad = {}^1\rho\cos\left({}^1\alpha^*(t) - {}^1\phi\right) + {}^1e_3^*(t){}^1u^*(t).\end{aligned} \tag{29}$$

The optimal control solution set is reduced to

$$\begin{aligned}{}^1u^*(t) &= -u_{\max}\mathrm{sign}({}^1e_3^*(t)) \quad |{}^1e_3^*(t)| > 0 \\ {}^1u^*(t) &\in [-u_{\max} \quad u_{\max}] \qquad {}^1e_3^*(t) = 0.\end{aligned} \tag{30}$$

The control input is uncertain when $|{}^1e_3^*(t)| = 0$. (1) If $|{}^1e_3^*(t)| = 0$ in the time interval $t \in [\zeta_1, \zeta_2] \subset [0, t_f]$, from (26), ${}^1\dot{e}_3^*(t) = {}^1\rho\sin({}^1\alpha^*(t) - {}^1\phi) = 0$, and from (22). ${}^1\mathcal{H}({}^1\mathbf{p}^*(t), {}^1\mathbf{e}^*(t), {}^1u^*(t)) = {}^1\rho\cos({}^1\alpha^*(t) - {}^1\phi) = 0$. Therefore, ${}^1\rho = 0$ and ${}^1\mathbf{e}(t) = \mathbf{0}$, which contradicts the precondition ${}^1\mathbf{e}(t) \neq \mathbf{0}$. (2) If $|{}^1e_3^*(t)| = 0$ exists only at certain isolated points, the control input at $|{}^1e_3^*(t)| = 0$ does not affect the final result.

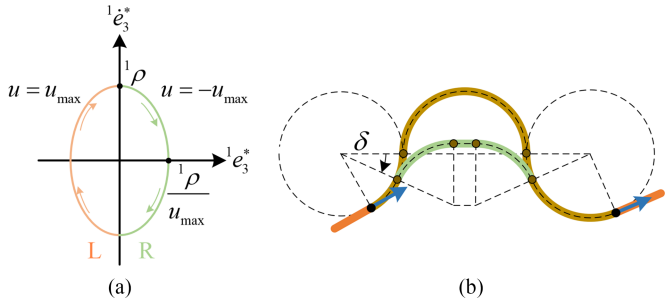

Fig. 6. Abnormal path. (a) Phase diagram, when ${}^1e_3^* > 0$, $u = -u_{\max}$, when ${}^1e_3^* < 0$, $u = u_{\max}$; hence, the transmission path is composed of arc R and L alternately. (b) Assuming that the path is in CCC type, a small enough δ can always be found for the nonoverlapping parts, the bending angle of the CCC path (brown path) is $\pi + 2\delta$, while the green path is $\pi - 2\delta$, therefore, the CCC path cannot be the minimum total bending angle path.

Therefore, the optimal control solution is the bang–bang control, substituting ${}^1u^*(t) = -u_{\max}\,\mathrm{sign}({}^1e_3^*(t))$ into (29)

$$\begin{aligned}&{}^1\mathcal{H}\left({}^1\mathbf{p}^*(t), {}^1e^*(t), {}^1u^*(t)\right) \\ &\quad = {}^1\rho\cos\left({}^1\alpha^*(t) - {}^1\phi\right) - |{}^1e_3^*(t)|u_{\max} = 0.\end{aligned} \tag{31}$$

By combining (26) and (31), the optimal costate function ${}^1e_3^*(t)$ satisfies the phase relationship

$$\left[|{}^1e_3^*(t)|u_{\max}\right]^2 + \left[{}^1\dot{e}_3^*(t)\right]^2 = \left[{}^1\rho\right]^2. \tag{32}$$

The phase diagram shown in Fig. 6(a) verifies that the abnormal path is bang–bang control and can only be in the form of CC or C, the bending angle of any arc does not exceed π, there is no minimum tension loss path in CCC type [see Fig. 6(b)]. From the solution set of Dubins path, it is also known that an abnormal path is the shortest.

(2) Normal path: When ${}^1e_0 > 0$, the Hamiltonian function is

$$\begin{aligned}&{}^1\mathcal{H}\left({}^1\mathbf{p}^*(t), {}^1\mathbf{e}^*(t), {}^1u^*(t)\right) \\ &\quad = {}^1e_0|{}^1u^*(t)| + {}^1\rho\cos({}^1\alpha^*(t) - {}^1\phi) + {}^1e_3^*(t){}^1u^*(t)\end{aligned} \tag{33}$$

(1) $|{}^1e_3^*(t)| = {}^1e_0$

If $|{}^1e_3^*(t)| = {}^1e_0$ only at some isolated points, then

$${}^1\mathcal{H}\left({}^1\mathbf{p}^*(t), {}^1e^*(t), {}^1u^*(t)\right) = {}^1\rho\cos({}^1\alpha^*(t) - {}^1\phi) = 0. \tag{34}$$

Therefore, ${}^1\rho = 0$ or ${}^1\rho \neq 0$, $\cos({}^1\alpha^*(t) - {}^1\phi) = 0$, and ${}^1\dot{e}_3^*(t) = {}^1\rho\sin({}^1\alpha^*(t) - {}^1\phi) = \pm{}^1\rho$.

If $|{}^1e_3^*(t)| = {}^1e_0$ at interval $t \in [\zeta_1, \zeta_2] \subset [0, t_f]$, then

$${}^1\dot{e}_3^*(t) = {}^1\rho\sin\left({}^1\alpha^*(t) - {}^1\phi\right) = 0. \tag{35}$$

To simultaneously satisfy (34) and (35), ${}^1\rho = 0$.

(2) $|{}^1e_3^*(t)| < {}^1e_0$

From (28), ${}^1u^*(t) = 0$, the Hamiltonian function needs to satisfy (34), then there is ${}^1\rho = 0$, or ${}^1\rho \neq 0$, ${}^1\dot{e}_3^*(t) = \pm{}^1\rho$.

(3) $|{}^1e_3^*(t)| > {}^1e_0$

Substituting ${}^1u^*(t) = -u_{\max}\,\mathrm{sign}({}^1e_3^*(t))$ into (33) yields

$$\begin{aligned}&{}^1\mathcal{H}\left({}^1\mathbf{p}^*(t), {}^1\mathbf{e}^*(t), {}^1u^*(t)\right) \\ &\quad = \left({}^1e_0 - |{}^1e_3^*(t)|\right)u_{\max} + {}^1\rho\cos({}^1\alpha^*(t) - {}^1\phi) = 0.\end{aligned} \tag{36}$$

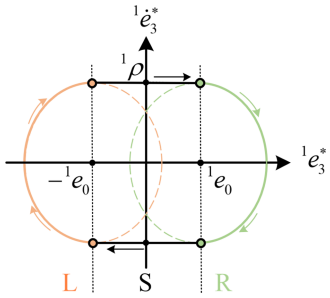

Fig. 7. Phase diagram of normal path with ${}^1\rho > 0$. When $|{}^1e_3^*| \le {}^1e_0$, ${}^1\dot{e}_3^* = \pm {}^1\rho$. When $|{}^1e_3^*| > {}^1e_0$, satisfy (37).

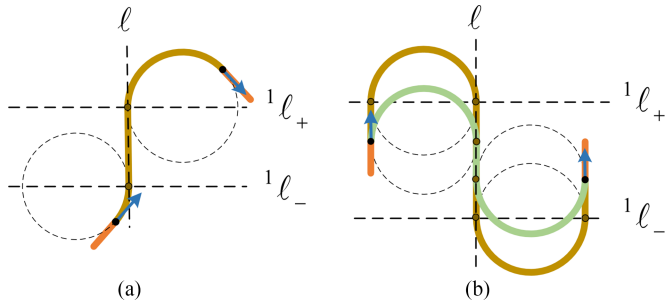

Fig. 8. Transmission path with different numbers of straight line segments. (a) CSC type (LSR). (b) SCSCS type (SRSLS).

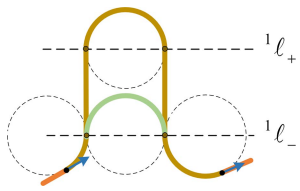

Fig. 9. CSCSC type transmission path.

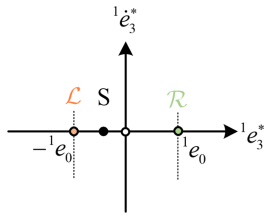

Fig. 10. Phase diagram of normal path with ${}^1\rho = 0$.

Combining (26) and (36), the optimal costate function ${}^1e_3^*(t)$ satisfies the phase relationship

$$\left[\left(|{}^1e_3^*(t)| - {}^1e_0\right) u_{\max}\right]^2 + \left[{}^1\dot{e}_3^*(t)\right]^2 = \left[{}^1\rho\right]^2. \tag{37}$$

In summary, the phase diagram contains two cases, corresponding to ${}^1\rho > 0$ or ${}^1\rho = 0$.

(1) ${}^1\rho > 0$

As shown in Fig. 7, the optimal transmission path is composed of arc C and straight line S alternately, and the bending angle of any arc does not exceed π. For the minimum tension loss path, it can be determined from (25) that the optimal costate function satisfies ${}^1e_3 = {}^1e_2 x - {}^1e_1 y + {}^1c$, and define the straight line ${}^1\ell_+$ and ${}^1\ell_-$

$$\begin{aligned} {}^1\ell_+ &: \quad {}^1e_2 x - {}^1e_1 y + {}^1c = {}^1e_0 \\ {}^1\ell_- &: \quad {}^1e_2 x - {}^1e_1 y + {}^1c = -{}^1e_0 \end{aligned} \tag{38}$$

where, ${}^1c$ denotes an arbitrary constant.

The control law in (28) indicates that the transmission path is a straight line in the area enclosed by ${}^1\ell_+$ and ${}^1\ell_-$, and the outer side is the arc with the maximum curvature. In segment S, from (34), the minimum tension loss path satisfies

$$\cos({}^1\alpha^*(t) - {}^1\phi) = 0. \tag{39}$$

Thus, ${}^1\alpha^*(t) = {}^1\phi \pm \frac{\pi}{2}$, where ${}^1\alpha^*(t)$ and ${}^1\phi$ are the direction angles of the straight part of the transmission path and the costate function line, respectively. Thus, the two are perpendicular to each other, and it is verified that the arc segment's bending angle cannot be greater than π.

When the number of straight-line segments in the transmission path is ≤ 1, the transmission path is in the form of CSC (RSL, LSR) and its subsets [see Fig. 8(a)]. Therefore, when the Dubins path solution set is CSC (RSL, LSR) and its subsets and all arc segments have bending angles $\le \pi$, the shortest path is equivalent to the minimum tension loss path.

When the number of straight-line segments of the transmission path is ≥ 2, the transmission path always contains the SCS form, as shown in Fig. 8(b), which is the SCSCS form, because the bending angle of the SCS segment is equal to π, the same bending angle path of CSC or CC type can always be found (the green path). In this case, the shortest path is a subset of the path with the minimum tension loss.

Proposition 1: The number of arc segments of the minimum tension loss path ≤ 2.

Proof: Assuming that the path is in the form of CSCSC (see Fig. 9), the bending angle of the middle section is π; hence, the minimum tension loss path can be equivalent to CCC type, at this time, there must be a path with a smaller total bending angle [see Fig. 6(b)], which is contradictory, Therefore, there is no path in the form CSCSC for minimum tension loss.

(2) ${}^1\rho = 0$

From (25) and (26), ${}^1e_1^*(t) = 0$, ${}^1e_2^*(t) = 0$, ${}^1\dot{e}_3^*(t) = 0$; hence, ${}^1e_3^*(t)$ is constant and ${}^1e_3^*(t) \neq 0$, there are three independent states in the phase diagram (see Fig. 10), corresponding to the three forms of the solution set as follows.

The form of $\mathcal{R}$, ${}^1e_3^*(t) = {}^1e_0$, indicates that the transmission path always rotates clockwise

$${}^1u^*(t) \in [-u_{\max} \quad 0]. \tag{40}$$

The form of $\mathcal{L}$, ${}^1e_3^*(t) = -{}^1e_0$, indicates that the transmission path always rotates counterclockwise

$${}^1u^*(t) \in [0 \quad u_{\max}]. \tag{41}$$

The form of S is a straight line $0 < |{}^1e_3^*(t)| < {}^1e_0$

$${}^1u^*(t) = 0. \tag{42}$$

When the solution set is in the form of $\mathcal{R}$ or $\mathcal{L}$, because ${}^1e_3^*(t) = {}^1e_0$ is in the continuous interval, the control input is

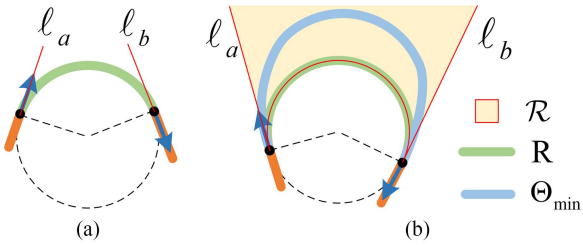

Fig. 11. Minimum tension loss path when the shortest path is R type. (a) Bending angle $< \pi$. (b) Bending angle $> \pi$, $\Theta_{\min}$ is one of the paths satisfying the solution set $\mathcal{R}$.

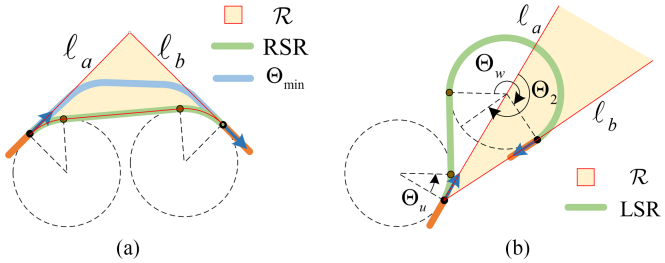

Fig. 12. Minimum tension loss path when the shortest path is CSC type. (a) Both sides of the S rotate in the same direction, RSR. (b) Both sides of the S rotate in different directions, LSR.

indeterminate. For example, when the Dubins path is in the form of R, because of R $\in \mathcal{R}$, if the bending angle is less than π, it is also the minimum tension loss path and is unique. If the bending angle is greater than π, the solution set of $\mathcal{R}$ is the area surrounded by the shortest path R, initial direction ℓ_a, and end direction straight line ℓ_b (see Fig. 11).

Similarly, when the shortest path is in the form of CSC and both sides of S rotate in the same direction (RSR or LSL), because of RSR $\in \mathcal{R}$, the Dubins path is the boundary of the solution set, which also satisfies the minimum tension loss. The $\mathcal{R}$ solution set comprises the area surrounded by ℓ_a, ℓ_b, and RSR [see Fig. 12(a)].

When the shortest path is in the form of CSC and both sides of S rotate in different directions (LSR or RSL), if there is an arc segment bending angle greater than π, the shortest path does not meet the minimum tension loss. For example, the shortest path is $L_u S R_w$ [see Fig. 12(b)] type, the total bending angle is $\Theta_1 = \Theta_u + \Theta_w$, where $\Theta_w > \pi$. The minimum tension loss path $\mathcal{R}$ solution set is surrounded by the initial and final directions ℓ_a, ℓ_b, and the line connecting the initial and final positions. The total bending angle of $\mathcal{R}$ is Θ_2, and $\Theta_2 = \Theta_1 - 2\Theta_u < \Theta_1$.

There is no path of minimum tension loss in the form of CCC when the shortest path is CCC type, as shown in Fig. 13, the bending angle of $L_u R_v L_w$ path is $\Theta_1 = \Theta_u + \Theta_v + \Theta_w$. The solution set of $\mathcal{L}$ is the area enclosed by the straight lines comprises the area surrounded by ℓ_a, ℓ_b, ℓ'_a, ℓ'_b, and parts of the LRL path, where $\ell_a // \ell'_a$, $\ell_b // \ell'_b$, and its The total bending angle is $\Theta_2 < \Theta_v < \Theta_1$.

Therefore, for the minimum tension loss path:

1) if the shortest path is CSC (RSR, LSL) form and its subsets, then the transmission path is in the form of $\mathcal{R}$ or $\mathcal{L}$, and the shortest path satisfies the minimum tension loss;

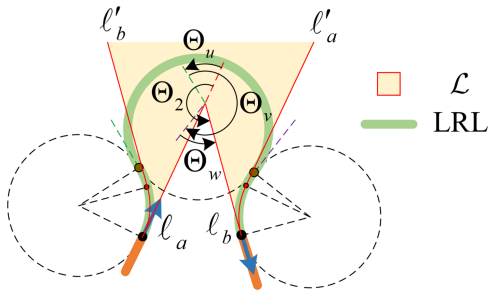

Fig. 13. Minimum tension loss path when the shortest path is CCC type.

2) if the shortest path is in the form of CSC (LSR, RSL) or CCC and its subsets, and if the bending angle of all arc segments is less than π, the shortest path is the minimum tension loss path. However, if there is an arc-segment bending angle greater than π, the transmission path is $\mathcal{R}$ or $\mathcal{L}$ form.

C. Minimum Tendon Deformation Path

The displacement transfer model yields the deformation of the tendon owing to changes in the tension distribution, and the minimum tendon deformation path objective function is to minimize the equivalent tendon length, from (9)

$$J_2 = \int_0^{t_f} \exp\left(-\mu_c \int_0^t |u(\tau)|\, d\tau\right) dt. \tag{43}$$

The Hamilton function is constructed

$$^2\mathcal{H}\left(\mathbf{p}(t), {}^2\mathbf{e}(t), {}^2u(t)\right) = {}^2e_0 \exp\left(-\mu_c \int_0^t |{}^2u(\tau)|\, d\tau\right) + {}^2\rho\cos({}^2\alpha^*(t) - {}^2\phi) + {}^2e_3(t)\,{}^2u(t). \tag{44}$$

Optimize input $^2u(t) \in [-u_{\max}, u_{\max}]$ to minimize Hamilton function $^2\mathcal{H}(^2\mathbf{p}^*(t), {}^2\mathbf{e}^*(t), {}^2u(t))$ and obtain $^2u^*(t)$ by

$$\arg\min\left({}^2e_0 \exp\left(-\mu_c \int_0^t |{}^2u(\tau)|\, d\tau\right) + {}^2e_3^*(t)\,{}^2u(t)\right). \tag{45}$$

When $^2e_0 = 0$, similar to the minimum tension loss path, the transmission path is an abnormal path and in the form of CC or C. When $^2e_0 > 0$, the transmission path is normal path. It can be found that when $^2u^*(t) = -u_{\max}\,\mathrm{sign}(^2e_3^*(t))$, both items $^2e_0 \exp(-\mu_c \int_0^t |^2u(\tau)|d\tau)$ and $^2e_3^*(t)\,^2u(t)$ in (45) satisfy the minimum condition. Therefore.

1) when the shortest path is CCC form and its subset, it is bang–bang control, the straight line ℓ divides the path into two parts, and the transmission path always rotates according to the maximum curvature (see Fig. 14). The shortest path is the minimum tendon deformation path.
2) if the shortest path is in the form of CSC or its subset, the shortest path contains straight-line segments, and the optimal solution set cannot be obtained directly through the minimum principle. The minimum tendon deformation path is the maximum curvature microarc "$\mathbb{S}$" that infinitely approximates a straight line, which does not exist. the detailed proof process can be found in Appendix A.

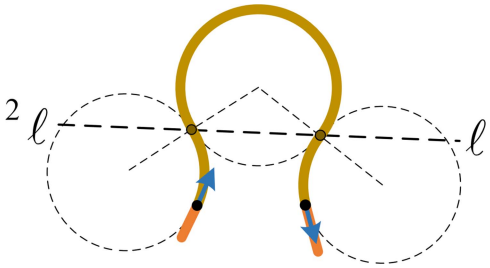

Fig. 14. Shortest path of CCC type is also the minimum tendon deformation path.

Therefore, it can be concluded that if the shortest path does not contain straight-line segments, it is also the minimum tendon deformation path. However, if the shortest path contains straight-line segments, then the minimum tendon deformation path does not exist.

IV. Coupling Transmission Path and Numerical Simulation

The minimum tension loss and tendon deformation were obtained independently under the same input. In applications with large loads, such as exoskeleton robots, tension transmission is more important, and in situations that require delicate operations, such as surgical robots, displacement transmission is more important. There are also occasions where both force and displacement are required, but they are coupled. The minimum tendon deformation path in the previous section was based on the same tension input, but the tension transfer was not optimal.

Finding a curve that satisfies both optimization objectives simultaneously is best, but it may be challenging to find an optimal solution. To some extent, the two optimization objectives are contradictory. For example, the path obtained by considering only the minimum tendon deformation does not constrain the transmission of tension; the more the path is bent, the greater the tension loss, and the smaller the tension on the output side. In [34], a scaling factor $S = \exp(-\mu\varsigma\beta)$ was introduced to reduce tendon deformation by increasing the bending on the input side and comparing the tendon deformations under the same tension input.

A. Tension Transfer Priority Path

In practical applications, the output force is typically determined by the load, and the input force is determined according to the tension transmission efficiency to select the motor type. A more significant input force is required to satisfy the load demand if the tension transfer efficiency is low. However, a motor with a higher output force has a higher cost, and excessive friction increases tendon loss and the possibility of breaking. Nevertheless, tendon deformation can be compensated for by motion control, which is relatively easier to achieve. Therefore, it is more reasonable to determine the minimum tendon deformation for the same tension output requirement. Finally, the principle of optimizing the tendon transmission path is as follows: first, ensure the minimum tension loss, and second, find the path with the minimum tendon deformation among all the paths with the minimum tension loss.

Corresponding to the minimum tension loss in Section III, the solution set is divided into two cases:

1) if ${}^2\rho > 0$, then all the minimum tension loss paths can find the corresponding form of the shortest path. The shortest path is the minimum tendon deformation path;
2) if ${}^2\rho = 0$, the solution set is in the form of $\mathfrak{C}$ ($\mathcal{R}$ or $\mathcal{L}$), for example, when the solution set is $\mathcal{L}$, the range of the control input $u(t)$ is further reduced.

Let ${}^3u(t) \in {}^2u^*(t) = [0, u_{\max}]$, and $\int_0^t |{}^2u(\tau)|d\tau = \alpha(t) - \alpha(0)$, define the objective function as

$$J_3 = \int_0^{t_f} \exp\left(-\mu_c\left(\alpha(t) - \alpha(0)\right)\right) dt. \tag{46}$$

The Hamilton function is constructed

$$\begin{aligned} &{}^3\mathcal{H}\left(\mathbf{p}(t), {}^3\mathbf{e}(t), {}^3u(t)\right) \\ &\quad = {}^3e_0\lambda(t) + {}^3\rho\cos({}^3\alpha(t) - {}^3\phi) + {}^3e_3(t){}^3u(t) \end{aligned} \tag{47}$$

where, $\lambda(t) = \exp(-\mu_c({}^3\alpha(t) - \alpha(0)))$.

Subsequently, optimize input ${}^3u(t) \in [0, u_{\max}]$ to minimize the Hamilton function ${}^3\mathcal{H}({}^3\mathbf{p}^*(t), {}^3\mathbf{e}^*(t), {}^3u(t))$, and

$${}^3u^*(t) = \arg\min\ \left({}^3e_3^*(t){}^3u(t)\right). \tag{48}$$

The optimal input is

$$\begin{aligned} &{}^3u^*(t) = 0 && {}^3e_3^*(t) > 0 \\ &{}^3u^*(t) \in [0 \quad u_{\max}] && {}^3e_3^*(t) = 0 \\ &{}^3u^*(t) = u_{\max} && {}^3e_3^*(t) < 0. \end{aligned} \tag{49}$$

Simultaneously, the optimal costate ${}^3\mathbf{e}^*$ satisfies

$${}^3\dot{e}_3^*(t) = {}^3e_0\mu_c\lambda^*(t) + {}^3\rho\sin\left({}^3\alpha^*(t) - {}^3\phi\right). \tag{50}$$

When ${}^3e_0 = 0$, the transmission path is an abnormal path and in the form of CC or C. When ${}^3e_0 > 0$, the transmission path is normal path, and

$$\begin{aligned} &{}^3\mathcal{H}\left({}^3\mathbf{p}^*(t), {}^3\mathbf{e}^*(t), {}^3u^*(t)\right) = {}^3e_0\lambda^*(t) \\ &\quad + {}^3\rho\cos({}^3\alpha^*(t) - {}^3\phi) + {}^3e_3^*(t){}^3u^*(t). \end{aligned} \tag{51}$$

If ${}^3e_3^*(t) = 0$ exists only at some isolated points, then the control input at ${}^3e_3^*(t) = 0$ does not affect the final result. If ${}^3e_3^*(t) = 0$ in a time interval $t \in [\zeta_1, \zeta_2] \subset [0, t_f]$, then

$$\begin{aligned} &{}^3\dot{e}_3^*(t) = {}^3e_0\mu_c\lambda^*(t) + {}^3\rho\sin({}^3\alpha^*(t) - {}^3\phi) = 0 \\ &{}^3\mathcal{H}\left({}^3\mathbf{p}^*(t), {}^3e^*(t), {}^3u^*(t)\right) \\ &\quad = {}^3e_0\lambda^*(t) + {}^3\rho\cos\left({}^3\alpha^*(t) - {}^3\phi\right) = 0. \end{aligned} \tag{52}$$

If (52) is satisfied, then there must be ${}^3\rho \neq 0$ and $\tan({}^3\alpha^*(t) - {}^3\phi) = \mu_c$. Therefore, the optimal control solution set contains straight-line segments, which is bang-singular control.

When ${}^3e_3^*(t) > 0$, ${}^3u^*(t) = 0$, and ${}^3\alpha_3^*(t), {}^3\dot{e}_3^*(t)$ are constants and have

$$\left[{}^3e_0\lambda^*(t)\right]^2 + \left[{}^3\dot{e}_3^*(t) - {}^3e_0\mu_c\lambda^*(t)\right]^2 = \left[{}^3\rho\right]^2. \tag{53}$$

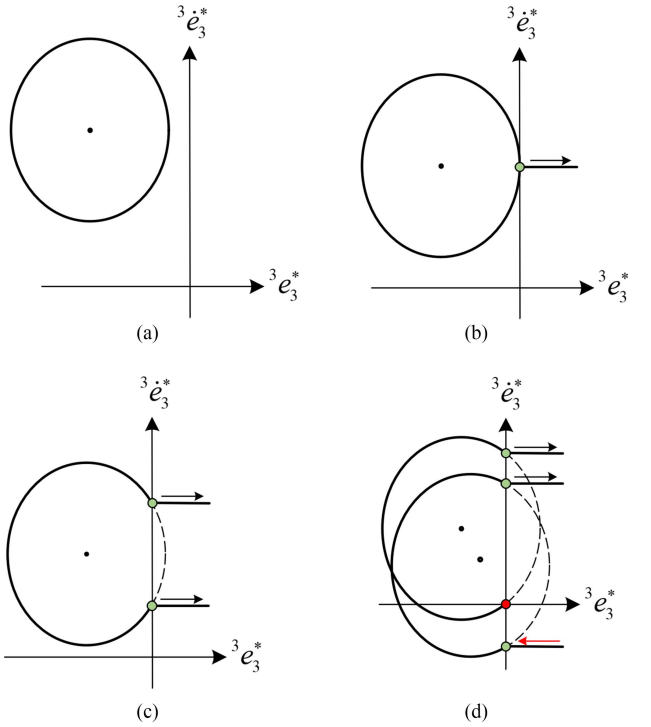

Fig. 15. Phase diagram of initial time t_0. (a) ${}^3\rho < {}^3e_0$. (b) ${}^3\rho = {}^3e_0$. (c) ${}^3\rho > {}^3e_0$. (d) Continued to increase ${}^3\rho$.

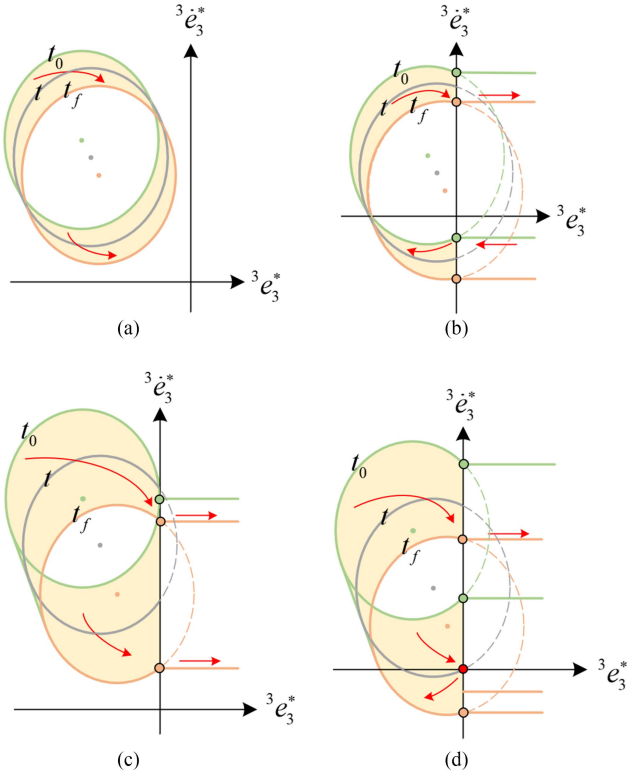

Fig. 16. Solution form, in the left phase plane, $u = u_{\max}$, the transmission path is L, in the right phase plane, $u = 0$, the transmission path is S. (a) L. (b) SLS. (c) LS. (d) LS or LSL.

When ${}^3e_3^*(t) < 0$, substituting ${}^3u^*(t) = u_{\max}$ into (47), combined with (50), the phase diagram at any moment t

$$\left[{}^3e_3^*(t)u_{\max} + {}^3e_0\lambda^*(t)\right]^2 + \left[{}^3\dot{e}_3^*(t) - {}^3e_0\mu_c\lambda^*(t)\right]^2 = \left[{}^3\rho\right]^2. \tag{54}$$

At the initial moment $t = t_0$, $\lambda^*(0) = 0$, then

$$\left[{}^3e_3^*(0)u_{\max} + {}^3e_0\right]^2 + \left[{}^3\dot{e}_3^*(0) - {}^3e_0\mu_c\right]^2 = \left[{}^3\rho\right]^2. \tag{55}$$

The center position of the ellipse is $(-\frac{{}^3e_0}{u_{\max}}, {}^3e_0\mu_c)$, according to the relative value of ${}^3e_0$ and ${}^3\rho$, there are four cases (see Fig. 15) : when $0 < {}^3\rho < {}^3e_0$, in the entire phase plane ${}^3e_3^*(t) < 0$, ${}^3u^*(t) = u_{\max}$; hence, the initial path form can only be L. When ${}^3\rho = {}^3e_0 > 0$, if ${}^3e_3^*(t) > 0$, ${}^3u^*(t) = 0$, as ${}^3\dot{e}_3^*(t) > 0$, The initial moment can only be selected in the left half plane; otherwise, the entire path is straight. The same situation occurred when ${}^3\rho > {}^3e_0 > 0$. However, with the increase in ${}^3\rho$, there is ${}^3\dot{e}_3^*(t) \le 0$ when ${}^3e_3^*(t) > 0$ thus, the initial path may be S, especially at (0,0). From (52), the only isolation point is the singular control.

At the termination time, $t = t_f$, as $\lambda^*(t_f) = \exp(-\mu_c\Theta) < 1$. The ellipse center coordinates $(-\frac{{}^3e_0\lambda^*(t_f)}{u_{\max}}, {}^3e_0\mu_c\lambda^*(t_f))$ move toward the origin, and the phase relationship satisfies

$$\left[{}^3e_3^*(t_f)u_{\max} + {}^3e_0\lambda^*(t_f)\right]^2 + \left[{}^3\dot{e}_3^*(t_f) - {}^3e_0\mu_c\lambda^*(t_f)\right]^2 = \left[{}^3\rho\right]^2. \tag{56}$$

Several possible forms of the transmission path are obtained from the relative positions of the phase diagrams at the initial and final times as follows. As shown in Fig. 16(a), in the entire phase plane, there is always ${}^3e_3^*(t) < 0$, corresponding to the transmission path of L form, Fig. 16(b) corresponds to the transmission path in SLS and its subset. When the transmission path is in SLS form, the bending angle of the middle section is greater than π, Fig. 16(c) corresponds to the transmission path in the form of LS and its subset, Fig. 16(d) corresponds to the transmission path in the form of LS, LSL, and its subset. A similar result was obtained for the $\mathcal{R}$ solution set.

According to the solution set form of the shortest path, the relationship among the minimum tension loss, minimum tendon deformation, and tension transfer priority path solution set can be obtained from Table III. Here, the shortest path's solution set is used for the classification because there are many methods for deriving the solution of the shortest path. The calculation of the shortest path mainly includes three methods: the geometric method [37], [39], minimum principle [40], [41], NLP dynamic programming [42], [43].

Therefore, the design steps of the tendon transmission path are as follows.

1) First, according to the given constraints, the shortest path is found, and the solution set is defined as ${}^1u^*$.
2) According to the form of the shortest path solution set, determine the solution set of the minimum tension loss path ${}^2u^*$. If the bending angle of all the arc segments of the shortest path is less than π, then ${}^1u^* = {}^2u^*$. If the shortest path has an arc segment bending angle greater than π, ${}^2u^*$ is in the form of $\mathfrak{C}$.
3) Find the minimum tendon deformation solution set in the minimum tension loss solution set, namely, ${}^3u^* \in {}^2u^*$. If

TABLE III
RELATIONSHIP BETWEEN DIFFERENT SOLUTION SETS

Dubins Path Form	Bending Angle	Minimum Tension Loss	Minimum Deformation	Tension Transfer Priority
C	$\forall < \pi$	C	C	C
	$= \pi$	C,SCS		
	$\exists > \pi$	$\mathfrak{C}$		
CS,SC	$\forall < \pi$	CS,SC	C $\mathbb{S}$,$\mathbb{S}$ C	CS,SC
	$= \pi$	CS,SC,SCS		
	$\exists > \pi$	$\mathfrak{C}$		
CC	$\forall < \pi$	CC	CC	CC
	$= \pi$	CC,SCSCS,SCSC,CSCS,$\mathfrak{C}$		
	$\exists > \pi$	$\mathfrak{C}$		SCS
CSC(RSL,LSR)	$\forall < \pi$	CSC	C$\mathbb{S}$C	CSC
	$= \pi$	CSC,SCSCS,SCSC,CSCS,$\mathfrak{C}$		
	$\exists > \pi$	$\mathfrak{C}$		SCS
CSC(RSR,LSL)		$\mathfrak{C}$	C$\mathbb{S}$C	CSC
CCC		$\mathfrak{C}$	CCC	SCS

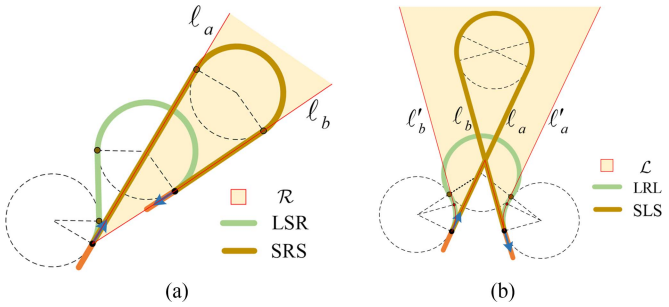

Fig. 17. SCS transmission path. (a) Shortest path is LSR, the minimum tension loss solution set is $\mathcal{R}$, the tension transfer priority path is SRS. (b) Shortest path is LRL, the minimum tension loss solution set is $\mathcal{L}$, and the tension transfer priority path is SLS.

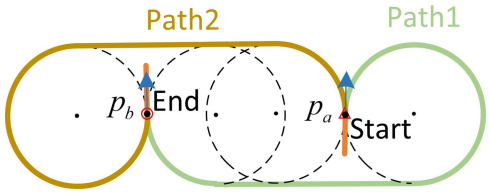

Fig. 18. Tension input from different side.

the minimum tension loss solution set is in the form of $\mathfrak{C}$, find the minimum tendon deformation transmission path in the form of SCS (see Fig. 17).

In particular, when the shortest path is CSC type, which is also the minimum tendon loss path (see Fig. 18). Path1 is in RSR form, and path2 is in LSL form, and the two paths have the same tension loss. If the input tension is on p_a side, path1 has less deformation, and if the input tension force is on the p_b side, the tendon deformation of path2 is the least.

B. Numerical Optimization Comparison

Pseudospectral method [44] is widely used in model predictive control and re-entry trajectory optimization. By discretizing the differential equations, the optimal control problem was transformed into a nonlinear constraint problem. The cost function is

$$J = \Phi\left(p\left(t_0\right), t_0, p\left(t_f\right), t_f\right) + \frac{t_f - t_0}{2} \int_{t_0}^{t_f} g\left(p(t), u(t), t; t_0, t_f\right) dt. \quad (57)$$

TABLE IV
DIFFERENT INITIAL AND TERMINAL STATES

Case	Initial State p_a	Terminal State p_b	κ_{max} (mm^{-1})	Dubins Path
Case1	$[0, 0, \frac{2}{3}\pi]$	$[-20, -10, \frac{4}{3}\pi]$	0.1	LR
Case2	$[0, 0, \frac{2}{3}\pi]$	$[-15, -30, \frac{4}{3}\pi]$	0.1	LSR
Case3	$[0, 0, \frac{2}{3}\pi]$	$[-10, -27.32, \frac{4}{3}\pi]$	0.1	LR
Case4	$[0, 0, \frac{2}{3}\pi]$	$[-5, -15, -\frac{2}{3}\pi]$	0.1	RSL
Case5	$[0, 0, \frac{2}{3}\pi]$	$[10, 4, -\frac{2}{3}\pi]$	0.1	LRL
Case6	$[0, 0, \frac{2}{3}\pi]$	$[20, 20, -\frac{2}{3}\pi]$	0.1	RSR

Table IV corresponds to the Dubins path of different initial states p_{t_0} and terminal states p_{t_f}, in which the direction angle remains unchanged, and the relative position changes. The state constraints: $p^{\min} = [-50, -50, -2\pi]$, $p^{\max} = [50, 50, 2\pi]$.

For the shortest path, we set the cost function with $\Phi = t_f$ and $g = 0$, the time constraint $t_f^{\text{limit}} = [0 \quad t_f^{\max}]$, and the control input constraint $u^{\text{limit}} = [-u^{\max} \quad u^{\max}]$, where $u^{\max} = 0.1$. For the path with the minimum total bending angle, we set the cost function with $\Phi = 0$ and $g = |u(t)|$; because the cost function contains the integral term, in some cases, when the transmission path is complex, it will take a long time to obtain the optimization result. Therefore, according to the shortest path optimization result J_1, the time constraint can be reduced to $t_f^{\text{limit}} = [J_1 \quad t_f^{\max}]$. For the minimum tendon deformation path, we set the cost function with $\Phi = 0$ and $g = \exp(-\mu_c \int_0^t |u(\tau)| d\tau)$.

When the shortest path is in the form of CC and the bending angle of all arc segments is less than π, it corresponds to an

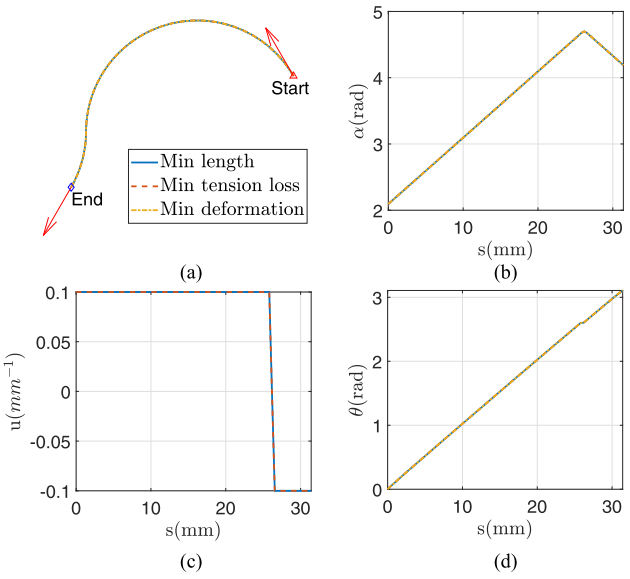

Fig. 19. Case1: Abnormal Path. (a) Transmission path. (b) Direction angle. (c) Control input. (d) Cumulative bending angle.

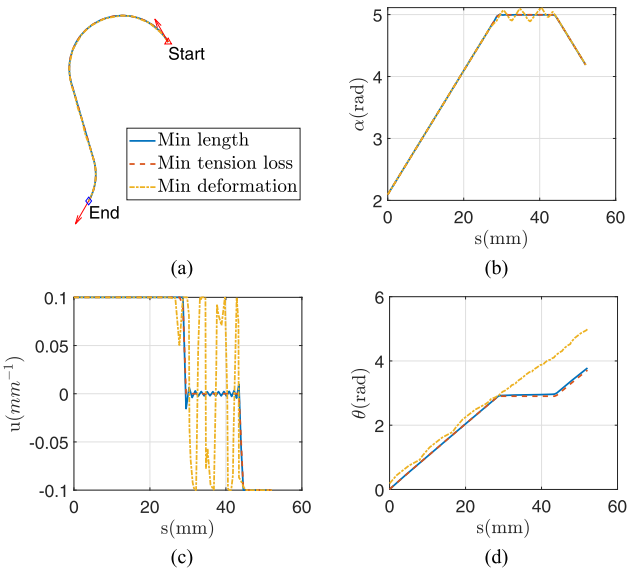

Fig. 20. Case2: Normal Path. (a) Transmission path. (b) Direction angle. (c) Control input. (d) Cumulative bending angle.

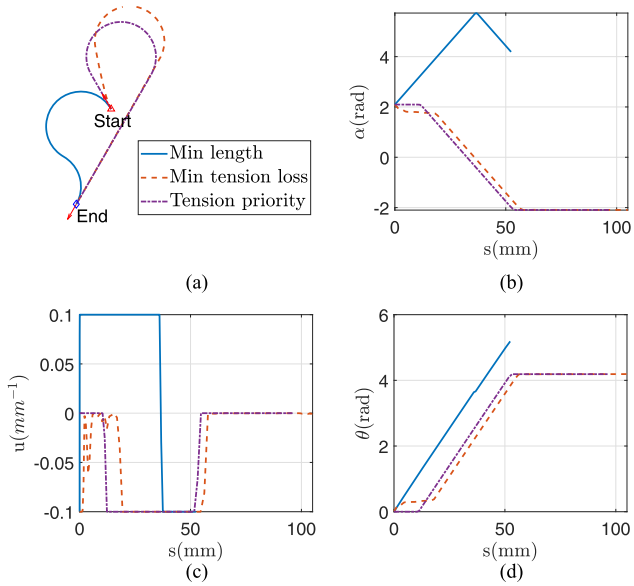

Fig. 21. Case3: LR form. (a) Transmission path. (b) Direction angle. (c) Control input. (d) Cumulative bending angle.

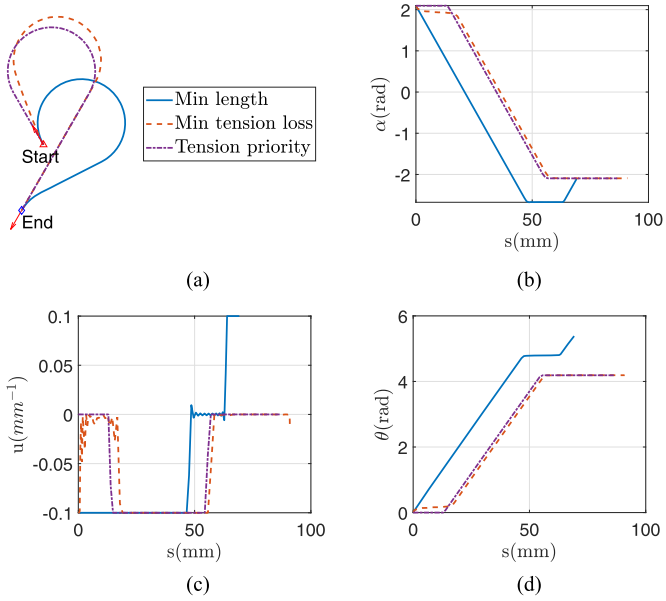

Fig. 22. Case4: RSL form. (a) Transmission path. (b) Direction angle. (c) Control input. (d) Cumulative bending angle.

abnormal path (see Fig. 19), which also satisfies the minimum tension loss and minimum tendon deformation; hence, the three transmission path optimization results are the same. The optimization results show that the transmission path is in LR form, the direction angle increases linearly from the initial $\frac{2}{3}\pi$ and then decreases linearly to the termination $\frac{4}{3}\pi$, the control input is always the maximum curvature, and the total bending angle increases linearly with the arc length.

For the normal path, when the shortest path contains straight line segments and the bending angles of all arc segments are less than π, the shortest path and minimum tension loss path are equivalent. However, for the minimum tendon deformation, there is a series of microarcs on the path with alternating rotations in different directions with the maximum curvature [see Fig. 20(a)]. Corresponding to the straight-line segment of the shortest path, the direction angle of the minimum tendon deformation path alternately changes. The control input jumps between the maximum and minimum values [see Fig. 20(b) and (c)], reducing deformation is at the cost of increasing the total bending angle [see Fig. 20(d)].

When there is an arc segment in the shortest path with a bending angle greater than π, the shortest paths are in the form of CC, CSC, and CCC (see Figs. 21, 22, and 23). At this time, the minimum tension loss solution set is in the form of $\mathcal{R}$; therefore, the solution that satisfies the minimum tension loss

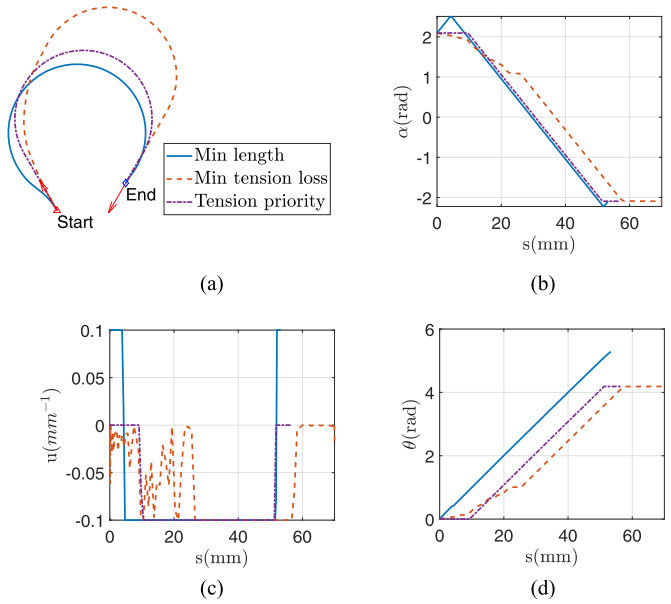

Fig. 23. Case5: LRL form. (a) Transmission path. (b) Direction angle. (c) Control input. (d) Cumulative bending angle.

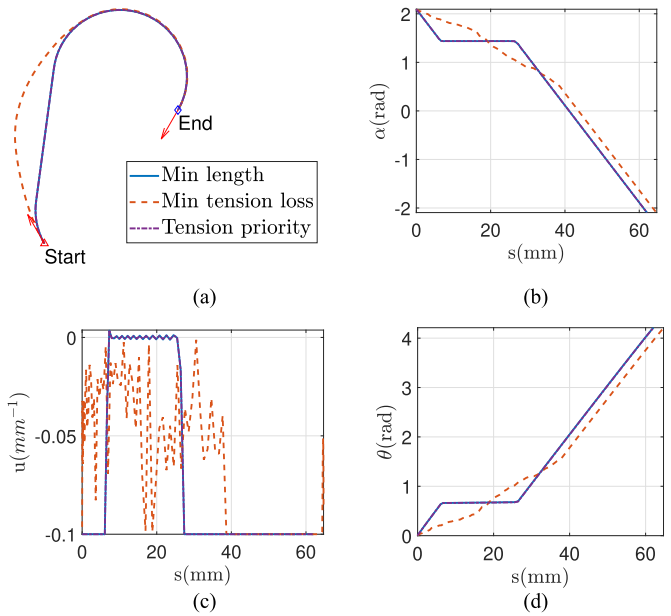

Fig. 24. Case6: RSR form. (a) Transmission path. (b) Direction angle. (c) Control input. (d) Cumulative bending angle.

is not unique, as shown in Figs. 21(c), 22(c), and 23(c), unlike the shortest path control input, which always takes the maximum or minimum value, the minimum tension loss curvature input is messy because there are infinitely many solutions that satisfy the minimum tension loss, as long as it is between $-u_{\max}$ and 0. For the tension transfer priority path, further reduce the control input limit to $u^{\text{limit}} = [-u^{\max} \quad 0]$. Then, the cost function is set to the minimum equivalent tendon length $g = \exp(-\mu_c(\alpha(t) - \alpha(t_0)))$, and the tension transmission priority path is in the form of SRS. In particular, as shown in Fig. 24, the shortest path is in the form of RSR, which itself is a form of $\mathcal{R}$ solution set; hence, the minimum tension loss path is $\mathcal{R}$ form.

TABLE V
SOLUTION SET FORM AND RESULTS

Dubins Path	Case	Cost Func	Solution Set Form	Actual Length (mm)	Bending Angle (rad)	Equivalent Length (mm)
CC ($\forall < \pi$)	Case1	①	LR	**31.41**	3.11	25.37
		②	LR	31.41	**3.11**	25.37
		③	LR	31.41	3.11	**25.37**
		④	LR	31.41	**3.11**	**25.37**
CSC ($\forall < \pi$)	Case2	①	LSR	**52.09**	3.78	38.70
		②	LSR	52.09	**3.71**	38.80
		③	L$\mathbb{S}$R	52.11	4.98	**37.50**
		④	LSR	52.09	**3.77**	**38.70**
CC ($\exists > \pi$)	Case3	①	LR	**52.39**	5.18	37.03
		②	$\mathcal{R}$	105.03	**4.19**	72.53
		③	LR	52.39	5.18	**37.03**
		④	SRS	96.56	**4.18**	**66.97**
CSC (RSL,LSR) ($\exists > \pi$)	Case4	①	RSL	**69.21**	5.38	45.46
		②	$\mathcal{R}$	90.93	**4.19**	65.16
		③	R$\mathbb{S}$L	70.40	6.83	**45.04**
		④	SRS	86.56	**4.18**	**62.35**
CCC	Case5	①	LRL	**53.30**	5.28	37.56
		②	$\mathcal{R}$	70.00	**4.18**	53.24
		③	LRL	53.30	5.28	**37.56**
		④	SRS	56.53	**4.18**	**43.94**
CSC (RSR,LSL)	Case6	①	RSR	**62.06**	4.21	49.83
		②	$\mathcal{R}$	64.71	**4.19**	52.31
		③	R$\mathbb{S}$R	62.62	6.03	**42.88**
		④	RSR	62.06	**4.20**	**49.85**

At this time, in the solution set $\mathcal{R}$, the shortest path is also the tension transmission priority path.

According to the classification of the Dubins path solution set, the six cases corresponded to different forms of the Dubins path. Specifically, we consider the ① shortest path, ② minimum tension loss, ③ minimum tendon deformation, and ④ tension transfer priority as optimization goals. Table V compares the specific path forms under the different optimization objectives mentioned previously and the corresponding actual lengths, total bending angles, and equivalent tendon lengths.

The influence of the curvature constraint on the transmission path is manifested in two ways in the following.

1) Corresponding to different forms of transmission paths. Because the path form is jointly determined by the relative size of the initial, terminal state, and curvature constraints, as shown in Table IV, the same curvature constraint is used. Different initial and terminal states correspond to different transmission path forms. Different terminal states are used for comparison to obtain the six path forms.
2) A similar form of transmission path but different transmission performance. Taking Case 2 in table IV as an example, because it is a CSC form transmission path, the shortest path, minimum tension loss path, and tension transmission priority path are the same. The curvature constraints $\kappa_{\max}$ were set to 0.33, 0.2, 0.15, and 0.1mm^{-1}, and the corresponding total bending angles were $2.59, 2.96, 3.12,$ and 3.78 rd, respectively (see

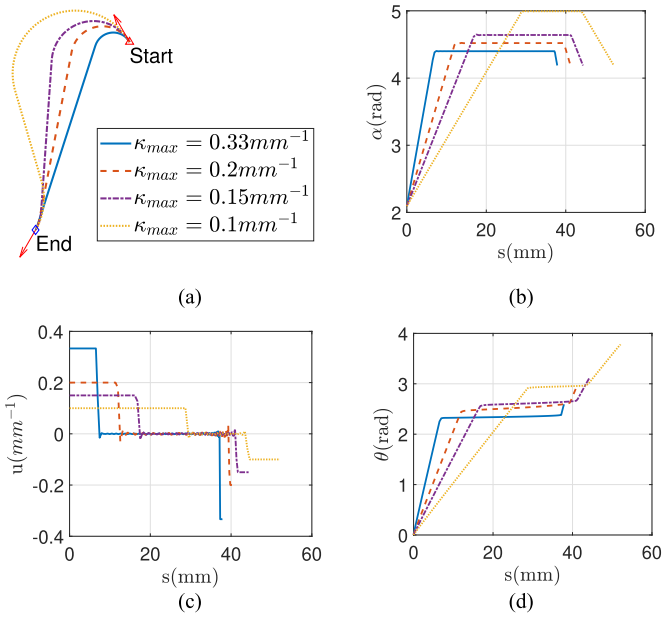

Fig. 25. Simulation of different curvature constraints. (a) Transmission path. (b) Direction angle. (c) Control input. (d) Cumulative bending angle.

Fig. 25). If continuing to decrease $\kappa_{\max}$, the transmission path takes the CCC form.

V. Optimal Design of a Tendon-Constrained Synchronous Rotation Mechanism

An n-degree-of-freedom cable-driven robot actuated by m cables can be classified as underconstrained ($m \leq n$) or fully constrained ($m \geq n+1$) [45]. Underactuated designs are often adopted to reduce the number of actuators. Among them, the closed cable loop is a feasible method that restricts equiangular rotation between different joints by tendons. For example, underactuated hands [46], deployment of solar panels [47], and large loop antennas [48]. It was mainly to realize the linkage of the plane, Liu [49] extended it to three-dimensional (3-D) space and proposed a tendon-constrained synchronous rotation mechanism. However, owing to the introduction of many connecting tendons, the friction between the tendon and sheath adversely affects the robot's performance. The phenomena of hysteresis and backlash caused by friction were analyzed in our previous study [50].

The tendon-driven manipulator is illustrated in Fig. 26. Through a synchronous rotation mechanism, the joints of each section were constrained to rotate at equal angles. The tendon-constrained synchronous rotation mechanism was used as the object to carry out the optimal design of the transmission path.

A. Basic Principle

The plane synchronous rotation mechanism comprises a pair of antagonistic tendons and four pulleys, called linkage tendon pairs, comprising two tendons arranged in a crossover around the pulley, with tendon anchor points fixed on the links on both sides. The pulley is mounted on the intermediate link and is concentric with the joint axis.

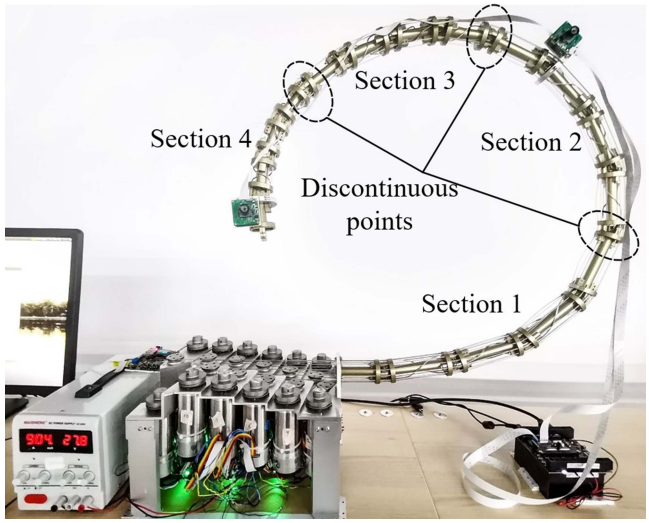

Fig. 26. Tendon-driven manipulator, each section contains four segments, the four segments rotate at equal angles, similar to the constant curvature bend of the continuum robot, to reduce the number of drivers.

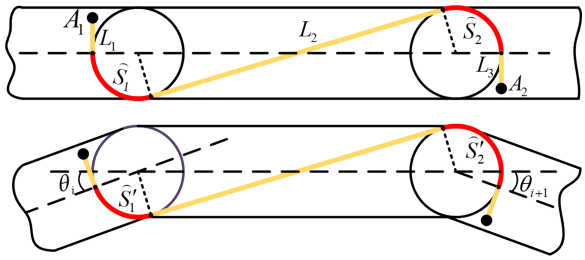

Fig. 27. Tendon-pulley synchronous rotation mechanism.

Considering one tendon as an example (see Fig. 27), when the joint rotates, only the length of the wind part of the tendon changes. Assuming that the manipulator is in a straight state, the lengths of the winding parts are $\widehat{S}_1$ and $\widehat{S}_2$, respectively. When joint i rotates angle θ_i, joint $i+1$ rotates angle θ_{i+1}, the winding part of becomes $\widehat{S}'_1 = \widehat{S}_1 - r\theta_i$, $\widehat{S}'_2 = \widehat{S}_2 + r\theta_{i+1}$, r is the pulley radius. Assuming that the total length of the tendon remains unchanged, $\widehat{S}'_1 + \widehat{S}'_2 = \widehat{S}_1 + \widehat{S}_2$. That is, $\theta_i = \theta_{i+1}$, and the adjacent joints rotate at equal angles.

To realize 3-D movement, the manipulator must achieve equiangular linkage in two directions. Simultaneously, for a tendon-driven slender manipulator, it is necessary to install tools, such as cameras. To facilitate the passage of power cables, the link is often designed in a hollow form; therefore, the transmission path is in the form of a tendon sheath wrapped around the link. Furthermore, to prevent hooking, the transmission path could not be exposed [see Fig. 28(a)].

The input and output of the tendon-sheath synchronous rotation mechanism are on the same plane and in the same direction, the relative positions of the initial and final points depend on the tendon winding radius R and the distance $2D$, and the radius of the cylindrical link is r [see Fig. 28(b)].

When the synchronous rotation mechanism is in a plane form, from the abovementioned transmission path design method, the

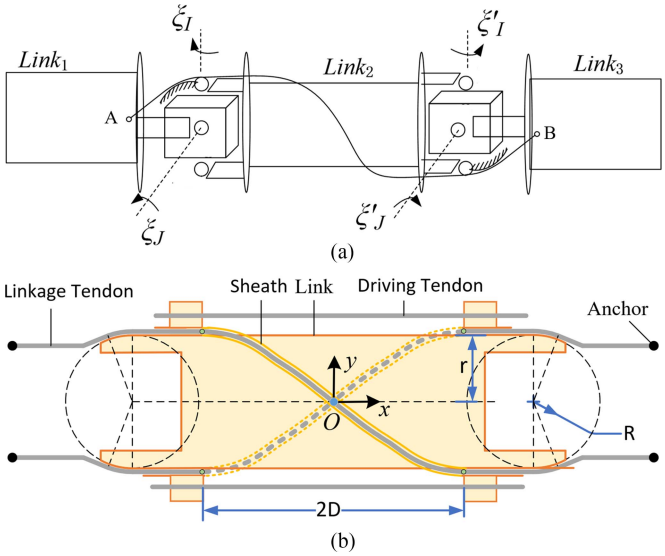

Fig. 28. Tendon-sheath synchronous rotation mechanism. (a) 3-D movement. (b) Basic component.

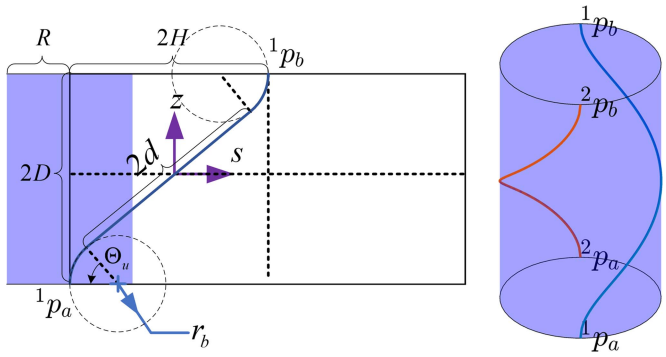

Fig. 29. Cylinder surface path and its expansion.

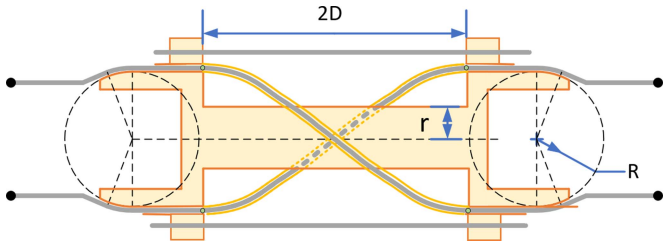

Fig. 30. Improved design: concentric cylinder with $r < R$.

CSC type transmission path can be obtained directly (See Appendix B for details and comparison with a polynomial curve). However, for the synchronous rotation mechanism, the sheath has a 3-D shape, and the shortest path problem in a 3-D situation has not been strictly proven. For the shortest path problem, Sussmann et al. [51] showed that each minimized segment in 3-D may also contain a helical form by using the maximum principle on the manifold. Therefore, for two points whose input and output directions are in the same plane, if the path can only be in plane, it must be a Dubins path. However, if the path can be in 3-D space, the shortest path may contain a spiral form. For the 3-D case, suboptimal paths are typically designed based on the 2-D Dubins path. The projection part of the 3-D trajectory on the horizontal plane was generated by the Dubins path planner to satisfy the curvature radius constraint, and a helical curve was constructed to satisfy the pitch angle constraint [52]. Váňa et al. [53] further decoupled the problem into separate 2-D paths in the horizontal and vertical planes and finally combined them into a feasible 3-D path.

B. Transmission Path Design

To reduce the influence of friction on the performance of the synchronous rotation mechanism, two tendon-sheath transmission paths were designed here, and the design of the synchronous rotation mechanism was improved. Finally, the transmission path in numerical form is obtained and compared with the designed tendon path.

Because the transmission path is constrained to the cylindrical surface where the link envelope is located, to obtain the parametric equation of the curve, the cylindrical surface is first expanded, and the curve passes through the points ${}^1p_a$, ${}^1p_b$, and satisfies the direction constraint at the endpoint; then, there is $H = \frac{\pi R}{2}$. The Dubins shortest path form is CSC form.

Helix curve parametric equation

$$
\begin{aligned}
x &= R\cos\left(\frac{s}{R}\right) \\
y &= R\sin\left(\frac{s}{R}\right) \\
z &= \begin{cases} -D + \sqrt{r_b^2 - (s + (H - r_b))^2} & s \in s_1 \\ \cot(\Theta_u)s & s \in s_2 \\ D - \sqrt{r_b^2 - (s - (H - r_b))^2} & s \in s_3 \end{cases}
\end{aligned} \tag{58}
$$

where, $s_1 = [-2H, -H - d\sin(\Theta_u)]$, $s_2 = [-H - d\sin(\Theta_u), -H + d\sin(\Theta_u)]$, $s_3 = [-H + d\sin(\Theta_u), 0]$, Θ_u, and d can be calculated by (68) similarly. Because the hollow link only needs to pass through a certain number of power cables, the radius of the link can be reduced (see Fig. 30), and the transmission path is in the area enclosed by two concentric cylinders.

The transmission path was designed, as shown in Fig. 31, It comprises the plane curve, the tangent line from the endpoint to the central cylinder, and the curve around the cylinder. The two plane paths are designed with the CS from Dubins curve, and the curve around the cylindrical surface is a Helix.

The Helix equation $c(\theta) = (r\cos\theta, r\sin\theta, v(\frac{\pi}{2} - \theta))$, at the connection point: $\theta_0 = a\cos(\frac{r}{R})$, the connection point coordinates $(r\cos\theta_0, r\sin\theta_0, v(\frac{\pi}{2} - \theta_0))$, direction $(-r\sin\theta_0, r\cos\theta_0, -v)$, the angle between the Helix and the Z-axis (0,0,1) is ϕ, and

$$\tan\phi = \frac{r}{v}. \tag{59}$$

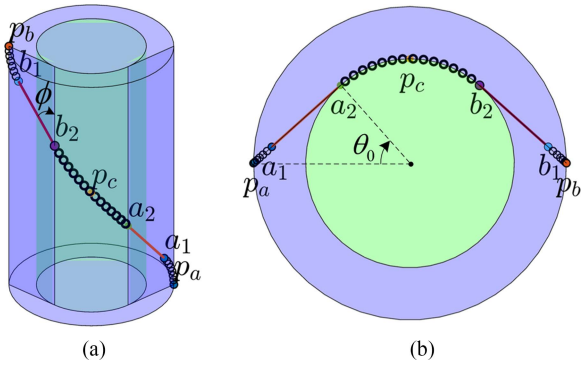

Fig. 31. Improved transmission path. (a) Dubins+Helix path. (b) Projection.

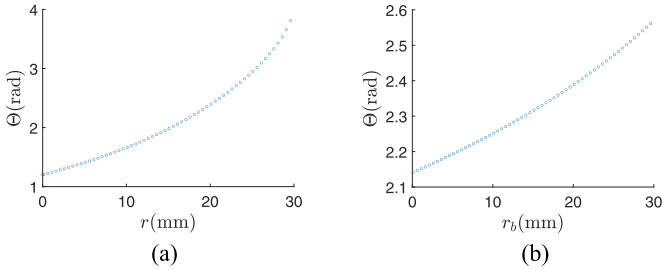

Fig. 32. Total bending angle. (a) Radius of the central cylinder r. (b) Maximum bending radius of the tendon r_b.

For the Dubins path

$$\tan\phi = \frac{\sqrt{R^2 - r^2} - r_b(1 - \cos\phi)}{D - v(\frac{\pi}{2} - \theta_0) - r_b \sin\phi}. \tag{60}$$

The Dubins and Helix paths are C^1 continuous at the connection point, with the same position and tangent direction, combining (59) and (60)

$$v = \frac{-Ds - r_b\sqrt{s^2 + D^2 - r_b^2}}{s^2 - r_b^2} r. \tag{61}$$

where, $s = r_b - \sqrt{R^2 - r^2} - r(\frac{\pi}{2} - \theta_0)$. The curvature of the Helix is given by

$$\kappa(\theta) = \frac{|c'(\theta) \times c''(\theta)|}{|c'(\theta)|^3} = \frac{r}{r^2 + v^2}. \tag{62}$$

Bending angle of the Helix with $\theta \in [\theta_0 \quad \pi - \theta_0]$

$$\Theta_s = \int_{\theta_0}^{\pi - \theta_0} \kappa(\theta)\sqrt{r^2 + v^2} d\theta = \frac{r}{\sqrt{r^2 + v^2}}(\pi - 2\theta_0). \tag{63}$$

Total bending angle of the path

$$\Theta = 2\phi + \Theta_s = 2a\tan\left(\frac{r}{v}\right) + \frac{r}{\sqrt{r^2 + v^2}}\left(\pi - 2a\cos\left(\frac{r}{R}\right)\right). \tag{64}$$

Fig. 32(a) is the relationship between the total bending angle and the radius of the central cylinder, when $r \to 0$, then $\frac{r}{v} \to \frac{(r_b - R)^2 - r_b^2}{-D(r_b - R) - r_b\sqrt{(r_b - R)^2 + D^2 - r_b^2}}$, this is the Dubins path, the minimum total bending angle is $\Theta = 2a\tan\left(\frac{R^2 - 2Rr_b}{-D(r_b - R) - r_b\sqrt{R^2 + D^2 - 2Rr_b}}\right)$. Fig. 32(b) is the relationship between the total bending angle and the tendon maximum bending radius. The radius of the central cylinder has a greater effect on the total bending angle.

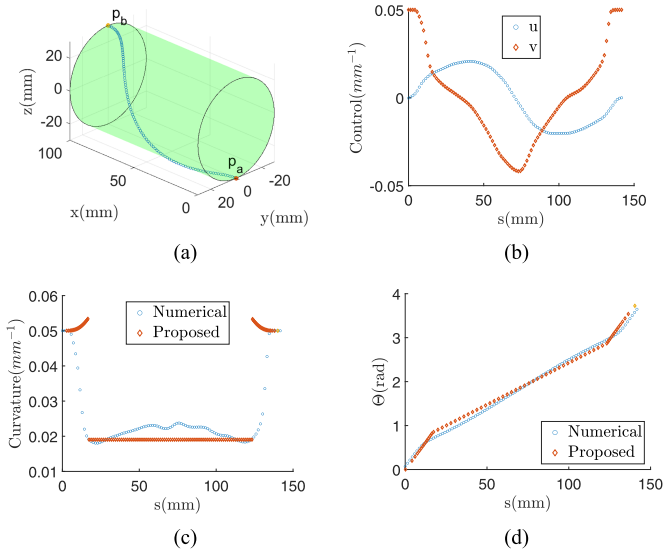

Fig. 33. Numerical optimization results (minimum bending angle) of Case 1, and are compared with the proposed transmission path. (a) Transmission path. (b) Control input. (c) Curvature. (d) Cumulative bending angle.

C. Numerical Simulation Verification

Similar to the plane particle, the 3-D space particle motion equation is represented by the following five parameters:

$$\dot{p}(t) = \begin{bmatrix} \dot{x}(t) \\ \dot{y}(t) \\ \dot{z}(t) \\ \dot{\alpha}(t) \\ \dot{\beta}(t) \end{bmatrix} = \begin{bmatrix} \cos\alpha(t)\cos\beta(t) \\ \cos\alpha(t)\sin\beta(t) \\ \sin\alpha(t) \\ u(t) \\ v(t) \end{bmatrix} \tag{65}$$

where, α and β denote the heading and pitch angles, respectively.

The curve parameter equation is $c(t) = [x(t) \quad y(t) \quad z(t)]^T$, and the relationship between the 3-D space direction angle and curvature is

$$\kappa(t) = \sqrt{u^2 + v^2\cos^2\alpha}. \tag{66}$$

Relevant simulation settings are as follows. Initial and end positions and directions: $p_{t_0} = [0, \ 0, \ -30, \ 0, \ 0]$ and $p_{t_f} = [100, \ 0, \ -30, \ 0, \ 0]$. State constraints: $p^{\min} = [0, \ 0, \ -30, \ 0, \ -1]$, $p^{\max} = [100, \ 30, \ 30, \ 1, \ 1]$. Control input constraints: $u_1^{\min} = [-0.05, -0.05]$, $u_2^{\max} = [0.05, 0.05]$.

Path and curvature constraints

$$C_1 = y^2 + z^2$$
$$C_2 = \sqrt{(u^2 + v^2\cos^2(\alpha))}. \tag{67}$$

TABLE VI
SYNCHRONOUS ROTATION MECHANISM TRANSMISSION PATH DESIGN

Design	Curve	Maximum Curvature (mm^{-1})	Actual Length (mm)	Total Bending Angle (rad)	Equivalent Length (mm)
Case1	Proposed (Dubins folding)	0.0534	140.40	3.73	109.02
	Numerical (Minimum length)	0.05	140.77	3.77	109.52
	Numerical (Minimum bending angle)	0.05	141.66	3.57	111.41
Case2	Improved (Dubins+helix)	0.05	126.96	2.39	106.69
	Numerical (Minimum length)	0.05	126.34	2.46	107.18
	Numerical (Minimum bending angle)	0.05	126.37	2.37	107.59

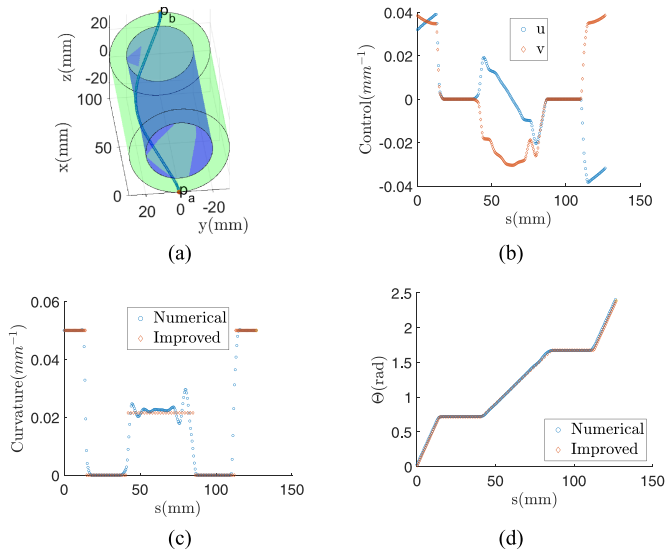

Fig. 34. Numerical optimization results (minimum bending angle) of Case 2, and are compared with the improved transmission path. (a) Transmission path. (b) Control input. (c) Curvature. (d) Cumulative bending angle.

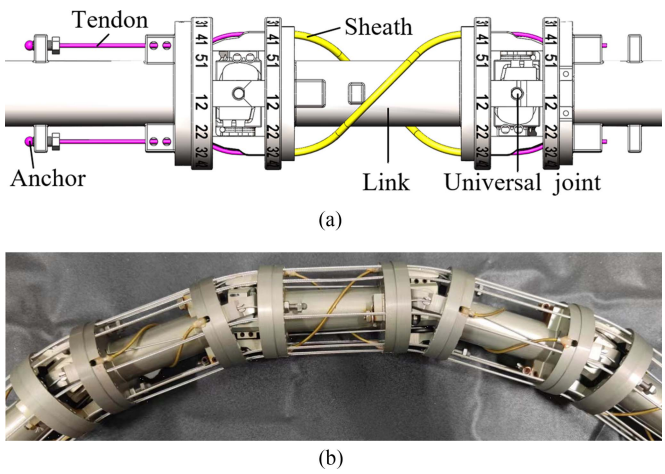

Fig. 35. Tendon-sheath synchronous rotation mechanism. (a) Design of synchronized rotation mechanism. (b) Equiangular rotation of adjacent joints.

The difference between the two simulation cases was that the path constraints were different.

Case 1: $C^{\min} = [900, 0]$, $C^{\max} = [900, 0.05]$.

Case 2: $C^{\min} = [400, 0]$, $C^{\max} = [900, 0.05]$.

Unlike the plane path with the control input which is always the maximum curvature bending, the control inputs of the cylindrical surface path change dynamically (see Fig. 33). The numerical optimization results have a similar form to the proposed Dubins folding path, the curvature is the largest on both sides, the middle section is close to the Helix (constant value), and the cumulative bending angle distribution is close.

For concentric cylindrical transmission paths, the control input is more complex. The improved transmission path includes the Dubins path and Helix. The curvature distribution mainly includes five segments and three forms: an arc with maximum curvature, a straight line, and a Helix. The numerical optimization results in Fig. 34 show that the designed transmission path is close to the optimal solution.

Table VI compares the maximum curvature, actual length, total bending angle, and equivalent lengths of the two designs. Because the space curve cannot directly constrain the curvature, the cylindrical surface transmission path can only constrain the curvature of the plane Dubins path, and the maximum curvature after folding is 0.0534, which exceeds the limit. Among them, the numerical method uses the shortest length and minimum total bending angle as the optimization objectives. The numerical optimization results show that for the synchronous rotation mechanism, there is little difference between the two (140.77 and 141.66°). Therefore, the shortest path can be used as the optimization objective to reduce the difficulty of solving transmission-path designs.

With the improved concentric cylinder design, the path length and total bending angle were significantly smaller, but the equivalent tendon length was the same, meaning that the tendon deformation was the same. The design of the synchronous rotation mechanism is shown in Fig. 35. In Case 1, the total bending angle of the Dubins folding path was 3.73 rad, in Case 2, the total bending angle of the Dubins + Helix path was 2.39 rad. Because the tension transfer mainly depends on the total bending angle, the improved transmission path design can significantly improve the force transmission performance by 36% (from 3.73 to 2.39 rad).

VI. CONCLUSION

In this study, the sheath path optimization problem is transformed into a curvature distribution optimization problem that satisfies specific constraints through the concept of the total bending angle and equivalent tendon length. Based on the optimal control theory and minimum principle, the solution sets

of different optimal target transmission paths are obtained. The important conclusions are as follows.

1) When an arc with a bending angle greater than π exists in the shortest path, the minimum tension loss solution set is in the form of $\mathfrak{C}$. If the bending angle of all arc segments in the shortest path is less than π, the path with the minimum tension loss is equivalent to the shortest path.
2) When the shortest path does not contain a straight-line segment, it is a subset of the minimum tendon deformation path. When there is a straight-line segment in the shortest path, minimum tension in the loss path does not exist.
3) Combined with the actual needs, the minimum total bending angle is taken as the first optimization objective, the path with the minimum tendon deformation is found on this basis. The solution sets are in the form of CSC, SCS, and their subsets.

Therefore, the design of the tendon transmission path is systematically expounded in theory, and it is an effective and low-cost solution to improve transmission performance by optimizing the transmission path. Based on the design method described previously, for a tendon-constrained synchronous rotation mechanism, 3-D transmission paths of the cylindrical surface and concentric cylinders were designed, and the influence of the link radius and tendon bending radius was analyzed. This is used to guide the optimal design of the tendon-constrained synchronous rotation mechanism, which reduces the friction force by 36%. A comparison with the numerical optimization results shows that the abovementioned 3-D transmission path design is close to the optimal solution.

In practical applications, there may be various restrictions on the setting of the sheath path, the sheath path optimization here provides a reference for the actual sheath path configuration. Examples include extending applications to three dimensions with piecewise optimal design, using the relationship between the Dubins path and different transmission path solution sets to simplify calculations, and using the proposed design theory to optimize the anchor points configuration in reverse. In the future, we will continue researching the optimal design of transmission paths with multiple intermediate anchor-point constraints.

Appendix A
Maximum Curvature Microarc

As shown in Fig. 36(a), knowing the initial position p_a, end position p_b, and direction of the sheath, first get its shortest path, which is composed of arcs and straight lines in the form of CS, the path length is $L_{\min}$, and L_1, L_2, L_3 are the maximum curvature paths of different lengths.

Fig. 36(b) corresponds to the dashed area in Fig. 36(a), the circle c_3 is tangent to c_1, c_2, and the straight line ℓ_2 divides the transmission path L_2 into two parts, on both sides of ℓ_2 are maximum curvature arc with different rotation direction. The circles c_4 and c_3 are symmetrical about ℓ_2, find the circles tangent to c_1 and c_4, and the circles tangent to c_2 and c_4, respectively. Another transmission path L_1 can be obtained, which is also the arc of maximum curvature on both sides of the straight line ℓ_1. In $\triangle BEC$, $BE + CE > BC$, $\overset{\frown}{BE} + \overset{\frown}{CE} > \overset{\frown}{BC}$ then, $\overset{\frown}{AB} + \overset{\frown}{BC} > \overset{\frown}{AB} + \overset{\frown}{BE} + \overset{\frown}{EC} = \overset{\frown}{DE} + \overset{\frown}{EC}$. Therefore, the transmission path length $L_1 < L_2$. As the straight line ℓ infinitely approaches the shortest path, the maximum curvature path length infinitely approximates $L_{\min}$. Therefore, the minimum tendon deformation path is the maximum curvature microarc "$\mathbb{S}$," which infinitely approximates the straight line.

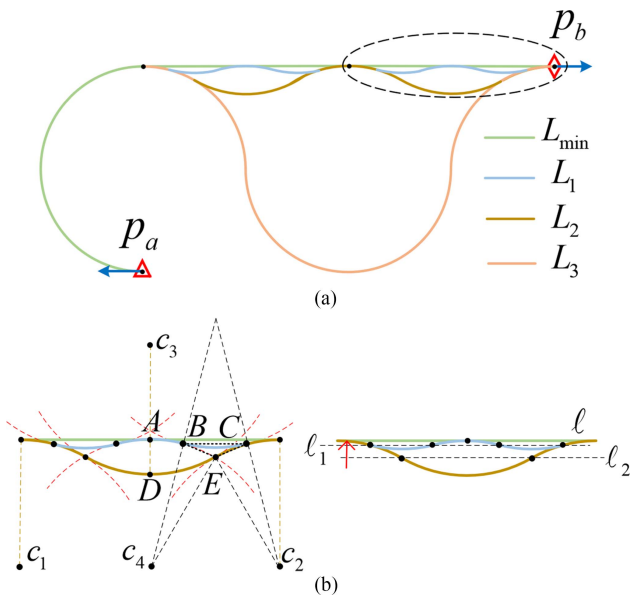

Fig. 36. Shortest path contains straight line segments. (a) Transmission paths of different lengths. (b) Maximum curvature path length $L_1 < L_2$.

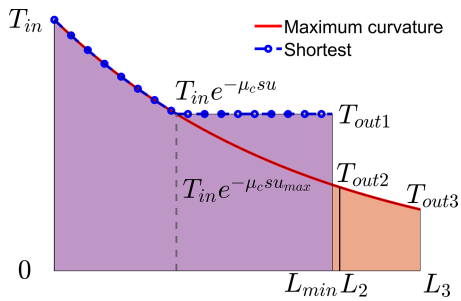

Fig. 37. Tension distribution along the tendon.

Assuming that the tension T_{in} is input on the p_a side, the tension distribution corresponding to the different sheath paths is shown in Fig. 37. where the total bending angle of the shortest path is π, which is also the minimum tension loss path; thus, the obtained tension T_{out1} is optimal, and the output tension of the maximum curvature path L_3 is T_{out3}.

The equivalent tendon length is linearly related to the tension integral. The shaded area represents the equivalent tendon length. The equivalent tendon length is related to the curvature distribution and also the integral length. Therefore, when the transmission path bends according to the maximum curvature and the length is equal to the shortest path, this is the lower limit of tendon deformation.

The tension loss is independent of the transmission direction, whereas the tendon deformation is related to the input side.

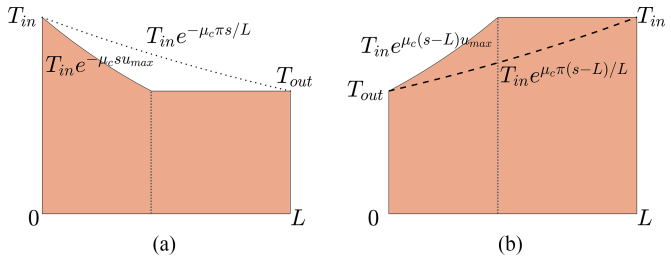

Fig. 38. Tension input on different sides, the dashed path is the path with average curvature π/L. (a) Pull the tendon on p_a side. (b) Pull the tendon on p_b side.

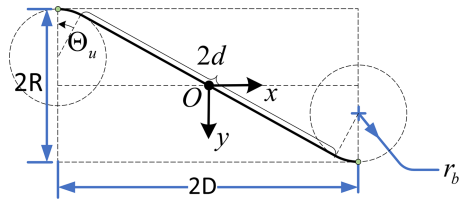

Fig. 39. Plane CSC type transmission path.

Taking the shortest path in Fig. 36(a) as an example, because the total bending angle is unchanged, the same pulling force T_{in} is input from any side, and the output T_{out} is the same. However, it can be seen from the shaded area that the tendon deformation inputs from different sides are different (see Fig. 38).

APPENDIX B
PLANE SYNCHRONOUS ROTATION MECHANISM TRANSMISSION PATH

When the synchronous rotation mechanism is in plane form, from the abovementioned transmission path design method, the CSC type transmission path can be obtained directly (see Fig. 39), r_b is the minimum bending radius of the tendon, the arc segment bending angle is Θ_u, the straight line segment length is $2d$, which satisfies the constraints

$$\begin{aligned} D &= r_b \sin(\Theta_u) + d\cos(\Theta_u) \\ R &= r_b(1-\cos(\Theta_u)) + d\sin(\Theta_u) \end{aligned} \tag{68}$$

where, $d = \sqrt{R^2 + D^2 - 2Rr_b}$, $\Theta_u = a\cos\left(\frac{Dd - r_b(R-r_b)}{r_b^2 + d^2}\right)$.

To compare the transmission performance more intuitively, we used a polynomial curve: $y = f(x) = \sum_{i=0}^{n} a_i x^i$, and the curve satisfies $f(-D) = -R, f(D) = R, f'(-D) = f'(D) = 0$ at the endpoint. The total bend angle correlates with the slope of the curve at zero and $\Theta = 2a\tan(f'(0))$, in the extreme case $\Theta_{\min} = 2a\tan(\frac{R}{D})$. We assume that the polynomial form is

$$f(x) = \frac{nR}{(n-1)D}x - \frac{R}{(n-1)D^n}x^n. \tag{69}$$

The curvature satisfies

$$k = \frac{|y''|}{(1+y'^2)^{\frac{3}{2}}} = \frac{\frac{nR}{D^n}x^{n-2}}{\left(1+\left(\frac{nR}{(n-1)D}\left(1-(\frac{x}{D})^{n-1}\right)\right)^2\right)^{\frac{3}{2}}}. \tag{70}$$

TABLE VII
TOTAL BENDING ANGLE AND MAXIMUM CURVATURE

Path	Polynomial degree n			Optimal path	
	3	5	7	CSC type	
Θ (rad)	1.466	1.287	1.221	1.201	1.177
κ_{max} (mm^{-1})	0.036	0.06	0.084	0.05	0.06

When $x = D$, the curvature is the largest, $k = \frac{nR}{D^2} \le k_{\max}$, to determine the degree of polynomial

$$n \le \frac{k_{\max} D^2}{R}. \tag{71}$$

As shown in Table VII, When $D = 50$ mm, $R = 30$ mm, if the curvature constraint is 0.05 mm^{-1}, the total bending angle of the CSC path is 1.201 rad. For polynomials, $n \le 4.17$, $n = 3$ (odd), $\Theta = 1.466$ rad. If $\kappa_{\max} = 0.06$ mm^{-1}, the total bending angle of the CSC path is 1.177 rad for polynomials $n \le 5$, $n = 5$, $\Theta = 1.287$ rad.

REFERENCES

[1] B. B. Kang, H. Choi, H. Lee, and K.-J. Cho, "Exo-glove poly II: A polymer-based soft wearable robot for the hand with a tendon-driven actuation system," *Soft Robot.*, vol. 6, no. 2, pp. 214–227, 2019.

[2] R. Roy, L. Wang, and N. Simaan, "Modeling and estimation of friction, extension, and coupling effects in multisegment continuum robots," *IEEE/ASME Trans. Mechatron.*, vol. 22, no. 2, pp. 909–920, Apr. 2017.

[3] F. Renda, M. Giorelli, M. Calisti, M. Cianchetti, and C. Laschi, "Dynamic model of a multibending soft robot arm driven by cables," *IEEE Trans. Robot.*, vol. 30, no. 5, pp. 1109–1122, Oct. 2014.

[4] M. T. Thai, P. T. Phan, T. T. Hoang, H. Low, N. H. Lovell, and T. N. Do, "Design, fabrication, and hysteresis modeling of soft microtubule artificial muscle (SMAM) for medical applications," *IEEE Robot. Automat. Lett.*, vol. 6, no. 3, pp. 5089–5096, Jul. 2021.

[5] W. Lai, L. Cao, J. Liu, S. C. Tjin, and L. Phee, "A three-axial force sensor based on fiber Bragg gratings for surgical robots," *IEEE/ASME Trans. Mechatron.*, vol. 27, no. 2, pp. 777–789, Apr. 2022.

[6] T. Do, T. Tjahjowidodo, M. W. S. Lau, and S. J. Phee, "An investigation of friction-based tendon sheath model appropriate for control purposes," *Mech. Syst. Signal Process.*, vol. 42, no. 1–2, pp. 97–114, 2014.

[7] U. Jeong, K. Kim, S.-H. Kim, H. Choi, B. D. Youn, and K.-J. Cho, "Reliability analysis of a tendon-driven actuation for soft robots," *Int. J. Robot. Res.*, vol. 40, no. 1, pp. 494–511, 2021.

[8] J. Hwangbo, V. Tsounis, H. Kolvenbach, and M. Hutter, "Cable-driven actuation for highly dynamic robotic systems," in *Proc. IEEE/RSJ Int. Conf. Intell. Robots Syst.*, 2018, pp. 8543–8550.

[9] V. Agrawal, W. J. Peine, and B. Yao, "Modeling of transmission characteristics across a cable-conduit system," *IEEE Trans. Robot.*, vol. 26, no. 5, pp. 914–924, Oct. 2010.

[10] U. Jeong and K.-J. Cho, "Control of a Bowden-cable actuation system with embedded BoASensor for soft wearable robots," *IEEE Trans. Ind. Electron.*, vol. 67, no. 9, pp. 7669–7680, Sep. 2020.

[11] H. Lee, B. B. Kang, and K.-J. Cho, "Branching tendon routing: A new tendon methodology for compact transmission," in *Proc. 14th Int. Conf. Ubiquitous Robots Ambient Intell.*, 2017, pp. 755–757.

[12] H. Ye, X. Feng, Y. Yabuki, S. Togo, Y. Jiang, and H. Yokoi, "Force-magnification mechanism with artificial tendon sheath for myoelectric prosthetic hand for children," in *Proc. IEEE Int. Conf. Robot. Biomimetics*, 2016, pp. 533–538.

[13] U. Jeong and K.-J. Cho, "Feedforward friction compensation of Bowden-cable transmission via loop routing," in *Proc. IEEE/RSJ Int. Conf. Intell. Robots Syst.*, 2015, pp. 5948–5953.

[14] W. Xu, H. Leung, P. W. Chiu, and C. C. Poon, "A feed-forward friction compensation motion controller for a tendon-sheath-driven flexible robotic gripper," in *Proc. IEEE Int. Conf. Robot. Biomimetics*, 2013, pp. 2112–2117.

[15] D. Chen, Y. Yun, and A. D. Deshpande, "Experimental characterization of Bowden cable friction," in *Proc. IEEE Int. Conf. Robot. Automat.*, 2014, pp. 5927–5933.
[16] K. Lau, E. Y. Leung, C. C. Poon, P. W. Chiu, J. Y. Lau, and Y. Yam, "Motion Compensation of Tendon-Sheath Driven Continuum Manipulator for Endoscopic Surgery," in *Proc. MATEC Web of Conf.*, 2015, vol. 32, Art. no. 04007.
[17] Y. Zhou, H. Liu, C. Wang, and Z. Wang, "Analysis on the force propagation of the tendon-sheath actuation in dexterous surgical robots," in *Proc. IEEE Int. Conf. Robot. Biomimetics*, 2016, pp. 731–736.
[18] S. Joshi, H. Sonar, and J. Paik, "Flow path optimization for soft pneumatic actuators: Towards optimal performance and portability," *IEEE Robot. Automat. Lett.*, vol. 6, no. 4, pp. 7949–7956, Oct. 2021.
[19] M. Kaneko, T. Yamashita, and K. Tanie, "Basic considerations on transmission characteristics for tendon drive robots," in *Proc. IEEE 5th Int. Conf. Adv. Robot. Robots Unstructured Environments*, 1991, pp. 827–832.
[20] Z. Wang, Z. Sun, and S. J. Phee, "Modeling tendon-sheath mechanism with flexible configurations for robot control," *Robotica*, vol. 31, no. 7, pp. 1131–1142, 2013.
[21] M. Tian, X. Wang, J. Wang, and Z. Gan, "Design of a lower limb exoskeleton driven by tendon-sheath artificial muscle," in *Proc. IEEE Int. Conf. Robot. Biomimetics*, 2019, pp. 2037–2042.
[22] A. T. Asbeck, S. M. De Rossi, I. Galiana, Y. Ding, and C. J. Walsh, "Stronger, smarter, softer: Next-generation wearable robots," *IEEE Robot. Automat. Mag.*, vol. 21, no. 4, pp. 22–33, Dec. 2014.
[23] S. Lee et al., "Autonomous multi-joint soft exosuit with augmentation-power-based control parameter tuning reduces energy cost of loaded walking," *J. Neuroengineering Rehabil.*, vol. 15, no. 1, pp. 1–9, 2018.
[24] J. Kim, J. Moon, S. Park, and G. Lee, "Characterizing force capability and stiffness of hip exosuits under different anchor points," *PLos One*, vol. 17, no. 8, 2022, Art. no. e0271764.
[25] M. Xiloyannis, D. Chiaradia, A. Frisoli, and L. Masia, "Physiological and kinematic effects of a soft exosuit on arm movements," *J. Neuroengineering Rehabil.*, vol. 16, no. 1, pp. 1–15, 2019.
[26] L. B. Bridgwater et al., "The Robonaut 2 hand-designed to do work with tools," in *Proc. IEEE Int. Conf. Robot. Automat.*, 2012, pp. 3425–3430.
[27] A. Wang, J. Ramos, J. Mayo, W. Ubellacker, J. Cheung, and S. Kim, "The HERMES humanoid system: A platform for full-body teleoperation with balance feedback," in *Proc. IEEE-RAS 15th Int. Conf. Humanoid Robots*, 2015, pp. 730–737.
[28] W. J. Marais and A. H. Göktogan, "Design and control of cram: A highly articulated cable-driven remote access manipulator for confined space inspection," in *Proc. Australas. Conf. Robot. Automat.*, 2017, pp. 9pg.
[29] Y. Jung and J. Bae, "Torque control of a double tendon-sheath actuation mechanism in varying sheath configuration," in *Proc. IEEE Int. Conf. Adv. Intell. Mechatron.*, 2017, pp. 1352–1356.
[30] H. Zhang, J. Li, K. Kong, and S. Wang, "System design of a novel minimally invasive surgical robot that combines the advantages of MIS techniques and robotic technology," *IEEE Access*, vol. 8, pp. 41147–41161, 2020.
[31] Q. Wu, X. Wang, L. Chen, and F. Du, "Transmission model and compensation control of double-tendon-sheath actuation system," *IEEE Trans. Ind. Electron.*, vol. 62, no. 3, pp. 1599–1609, Mar. 2015.
[32] Z. Sun, Z. Wang, and S. J. Phee, "Modeling and motion compensation of a bidirectional tendon-sheath actuated system for robotic endoscopic surgery," *Comput. Methods Programs Biomed.*, vol. 119, no. 2, pp. 77–87, 2015.
[33] S. Buchanan and F. Sergi, "Dynamic modeling and state estimation of cable-conduit actuation during interaction with non-passive environments," *IEEE/ASME Trans. Mechatron.*, vol. 26, no. 5, pp. 2462–2471, Oct. 2021.
[34] Z. Sun, Z. Wang, and S. J. Phee, "Elongation modeling and compensation for the flexible tendon–sheath system," *IEEE/ASME Trans. Mechatron.*, vol. 19, no. 4, pp. 1243–1250, Aug. 2014.
[35] C. R. Wagner and E. Emmanouil, "Efficiency and power limits of electrical and tendon-sheath transmissions for surgical robotics," *Front. Robot. AI*, vol. 5, 2018, Art. no. 50.
[36] M. Athans and P. L. Falb, *Optimal Control: An Introduction to the Theory and its Appl.*. Chelmsford, MA, USA: Courier Corporation, 2013.
[37] L. E. Dubins, "On curves of minimal length with a constraint on average curvature, and with prescribed initial and terminal positions and tangents," *Amer. J. Math.*, vol. 79, no. 3, pp. 497–516, 1957.
[38] S. Hota and D. Ghose, "Optimal geometrical path in 3D with curvature constraint," in *Proc. IEEE/RSJ Int. Conf. Intell. Robots Syst.*, 2010, pp. 113–118.
[39] A. M. Shkel and V. Lumelsky, "Classification of the Dubins set," *Robot. Auton. Syst.*, vol. 34, no. 4, pp. 179–202, 2001.
[40] X. C. Ding, A. R. Rahmani, and M. Egerstedt, "Multi-UAV convoy protection: An optimal approach to path planning and coordination," *IEEE Trans. Robot.*, vol. 26, no. 2, pp. 256–268, Apr. 2010.
[41] C. Y. Kaya, "Markov–Dubins path via optimal control theory," *Comput. Optim. Appl.*, vol. 68, no. 3, pp. 719–747, 2017.
[42] P. Bevilacqua, M. Frego, D. Fontanelli, and L. Palopoli, "A novel formalisation of the Markov-Dubins problem," in *Proc. IEEE Eur. Control Conf.*, 2020, pp. 1987–1992.
[43] J. Herynek, P. Váňa, and J. Faigl, "Finding 3 d Dubins paths with pitch angle constraint using non-linear optimization," in *Proc. IEEE Eur. Conf. Mobile Robots*, 2021, pp. 1–6.
[44] D. Garg, M. Patterson, W. W. Hager, A. V. Rao, D. A. Benson, and G. T. Huntington, "A unified framework for the numerical solution of optimal control problems using pseudospectral methods," *Automatica*, vol. 46, no. 11, pp. 1843–1851, 2010.
[45] G. Abbasnejad, J. Eden, and D. Lau, "Generalized ray-based lattice generation and graph representation of wrench-closure workspace for arbitrary cable-driven robots," *IEEE Trans. Robot.*, vol. 35, no. 1, pp. 147–161, Feb. 2019.
[46] R. Ozawa, K. Hashirii, Y. Yoshimura, M. Moriya, and H. Kobayashi, "Design and control of a three-fingered tendon-driven robotic hand with active and passive tendons," *Auton. Robots*, vol. 36, no. 1, pp. 67–78, 2014.
[47] B. Wie, N. Furumoto, A. Banerjee, and P. Barba, "Modeling and simulation of spacecraft solar array deployment," *J. Guid., Control, Dyn.*, vol. 9, no. 5, pp. 593–598, 1986.
[48] K. Fu et al., "From multiscale modeling to design of synchronization mechanisms in mesh antennas," *Acta Astronautica*, vol. 159, pp. 156–165, 2019.
[49] T. Liu et al., "Improved mechanical design and simplified motion planning of hybrid active and passive cable-driven segmented manipulator with coupled motion," in *Proc. IEEE/RSJ Int. Conf. Intell. Robots Syst.*, 2019, pp. 5978–5983.
[50] Y. Li, Y. Liu, D. Meng, X. Wang, and B. Liang, "Modeling and experimental verification of a cable-constrained synchronous rotating mechanism considering friction effect," *IEEE Robot. Automat. Lett.*, vol. 5, no. 4, pp. 5464–5471, Oct. 2020.
[51] H. J. Sussmann, "Shortest 3-dimensional paths with a prescribed curvature bound," in *Proc. IEEE 34th Conf. Decis. Control*, 1995, vol. 4, pp. 3306–3312.
[52] Y. Wang, S. Wang, M. Tan, C. Zhou, and Q. Wei, "Real-time dynamic Dubins-Helix method for 3-D trajectory smoothing," *IEEE Trans. Control Syst. Technol.*, vol. 23, no. 2, pp. 730–736, Mar. 2015.
[53] P. Váňa, A. A. Neto, J. Faigl, and D. G. Macharet, "Minimal 3D dubins path with bounded curvature and pitch angle," in *Proc. IEEE Int. Conf. Robot. Automat.*, 2020, pp. 8497–8503.

Yanan Li received B.S. degree in control science and engineering from Harbin Institute of Technology, Harbin, China, in 2014, and the M.S. degree in control engineering from the Department of Automation, Tsinghua University, Beijing, China, in 2018. He is currently working toward Ph.D. degree in mechanical engineering with the Harbin Institute of Technology, Harbin, China.

His research interests include cable-driven robots, contact modeling, and multibody system dynamics.

Weining Lu received the B.S. degree in physics from the Department of Physics, Fudan University, Shanghai, China, in 2007, and the Ph.D. degree in information science and technology from Tsinghua University, in 2017.

He is currently an Assistant Professor with the Department of Automation, Tsinghua University. His current research interest includes solving anomaly detection problems by using deep architecture networks, computer vision, and datamining.

Yu Liu received the Ph.D. degree in mechanical engineering from the Harbin Institute of Technology, Harbin, China, in 2004.

He is a Professor with the College of Mechanical and Electrical Engineering, Harbin Institute of Technology. His research interests include space robotics and parallel mechanism.

Deshan Meng (Member, IEEE) received the Ph.D. degree in control science and engineering from Harbin Institute of Technology Shenzhen Graduate School, Shenzhen, China, in 2017.

He is currently an assistant professor with the School of Aeronautics and Astronautics, Sun Yat-sen University, Shenzhen, P.R. China. His research interests include space robotics, cable-driven robots, and multibody system dynamics and control.

Xueqian Wang received the Ph.D. degree in control science and engineering from the Harbin Institute of Technology, Harbin, China, in 2010.

He is currently a Professor and the Leader with the Center of Intelligent Control and Telescience, Tsinghua Shenzhen International Graduate School, Tsinghua University, Shenzhen, China. His research interests include dynamics modeling, control, and teleoperation of robotic systems.

Bin Liang received the B.S. degree in control engineering from Northwestern Polytechnical University, Xi'an, China, in 1991, and the Ph.D. degree in precision instruments and mechanology from Tsinghua University, Beijing, China, in 1994.

He is a Professor with the Department of Automation, Tsinghua University. His research interests include space robots, manipulators, and intelligent control.

IEEE Transactions on Robotics (T-RO) paper, presented at ICRA 2024, Yokohama, Japan. Cite as T-RO paper.